TECHNISCHE
UNIVERSITÄT
WIEN
Vienna University of Technology

DIPLOMARBEIT

Bulk and Surface Characterization of $In_2O_3(001)$ Single Crystals

Ausgeführt am Institut für Angewandte Physik
der Techischen Universität Wien

unter der Anleitung von
Univ.Prof. Dipl.-Ing. Dr.techn. Ulrike Diebold

durch

Mag. Daniel Robert Hagleitner
Webgasse 6/24, 1060 Wien

Wien, am 11.11.2011 ______________________

Abstract

Indium oxide, In_2O_3, is an important semiconductor with a wide range of technical applications including transparent films for Organic Light Emitting Diodes (OLEDS) and Organic Photovoltaic Cells (OPVC), gas sensing, and transparent infrared reflectors. The present diploma thesis comprises a comprehensive bulk and surface investigation of high-quality $In_2O_3(001)$ single crystals. The transparent-yellow, cube-shaped single crystals were grown by the flux method. Measurements with an electron probe microanalyzer show that the crystals were grown using the fluxes B_2O_3 and PbO. Inductively coupled plasma mass spectrometry (ICP-MS) measurements revealed small residues of Pb, Mg and Pt in one of the crystals. Polarized light microscopy lead to the observation of multiple growth domains and stress birefringence. Four-point-probe measurements showed a resistivity of $2 \pm 0.5 \times 10^5$ Ω cm, which translates into a carrier concentration of surprisingly low 10^{12} cm^{-3}. The results from X-ray diffraction (XRD) measurements revise the lattice constant to 10.1150(5) Å from the previously accepted value of 10.117 Å. Scanning Tunneling Microscopy (STM) images of a reduced (sputtered/annealed) surface show a step height of 5 Å, which indicates a preference for one type of surface termination. A combination of low-energy ion scattering and atomically resolved STM indicates an indium-terminated surface with small islands of 2.5 Å height, which corresponds to a strongly distorted indium lattice. Scanning Tunneling Spectroscopy (STS) reveals a pronounced surface state at the Fermi level (E_F). Photoelectron Spectroscopy (PES) shows additional, deep-lying band gap states, which can be removed by exposure of the surface to activated oxygen. Oxidation also results in a shoulder at the O 1s core level at a higher binding energy, possibly indicative of a surface peroxide species. A downward band bending of 0.4 eV and an upward band bending of $\sim$0.1 eV is observed for the reduced and oxidized surfaces, respectively.

Kurzfassung

Indiumoxid, In_2O_3, ist ein wichtiger Halbleiter, der in vielen Bereichen industriell eingesetzt wird. Dazu gehören unter anderem transparente, leitfähige Schichten für organische Leuchtdioden (OLEDs) und organische Solarzellen, Gassensoren sowie transparente, infrarotes Licht reflektierende Beschichtungen. Die Diplomarbeit befasst sich mit den Festkörper- und Oberflächeneigenschaften von hochqualitativen $In_2O_3(001)$ Einkristallen. Die transparenten, gelblichen Kristalle sind kubisch geformt und wurden mittels der Flussmethode hergestellt. Messungen mit einer Elektronenstrahlmikrosonde bestätigen die Vermutungen, dass beim Wachstumsprozess B_2O_3 und PbO als Flussmittel verwendet wurden. Massenspektrometrie mit induktiv gekoppeltem Plasma (ICP-MS) zeigte, dass sich Rückstände von Blei, Magnesium und Platin in einem der Kristalle befinden. Unter polarisiertem Licht konnten Spannungsdoppelbrechung und mehrere Wachstumsdomänen beobachtet werden. Die Messung des spezifischen Widerstands mittels der Vierpunktmethode erlaubte die näherungsweise Abschätzung der Ladungsträgerkonzentration auf 10^{12} cm^{-3}, was auf einen hohen Reinheitsgrad der Kristalle hindeutet. Durch Röntgenbeugungsmessungen konnte die Gitterkonstante vom zuvor verwendeten Wert von 10.117 Å auf 10.1150(5) Å verfeinert werden. Rastertunnelmikroskopieaufnahmen der reduzierten Oberfläche (zur Präparation zerstäubt und wieder ausgeheilt) zeigen, dass alle Stufenkanten eine Höhe von 5 Å besitzen. Dies deutet darauf hin, dass es höchstwahrscheinlich nur eine Art von Kristallterminierung gibt. Die Kombination der Ergebnisse von Rastertunnelmikroskopie mit atomarer Auflösung sowie niederenergetischer Ionenstreuspektroskopie ermöglicht die Gewinnung weiterer Erkenntnisse: Die reduzierte Oberfläche ist mit hoher Wahrscheinlichkeit Indium- und nicht Sauerstoff terminiert. In den Bildern mit atomarer Auflösung sind kleine, 2.5 Å hohe Inseln zu erkennen, die als ein stark verzerrtes Indiumgitter interpretiert werden können. Durch den Einsatz von Rastertunnelspektroskopie konnte gezeigt werden, dass es einen ausgeprägten Oberflächenzustand bei der Fermienergie gibt. Photoelektronenspektroskopie zeigte weitere, tief liegende Zustände in der Bandlücke, welche durch Oxidation der Oberfläche mit atomaren Sauerstoff entfernt werden konnten. Die Oxidation führt darüberhinaus zu einer Schulter des O 1s Orbitals auf der Seite mit höherer Bindungsenergie. Dies ist vermutlich auf die Bildung von Peroxiden an der Oberfläche zurückzuführen. Die reduzierte Oberfläche zeigt des Weiteren ein aufwärts gerichtetes Band Bending im Ausmaß von etwa 0.4 eV. Die oxidierte Oberfläche hingegen besitzt ein abwärts gerichtetes Band Bending von ca. 0.1 eV.

Contents

Acronyms

AES	Auger Electron Spectroscopy
ARPES	Angle-resolved photoemission spectroscopy
BZ	Brillouin zone
CB	Conduction Band
CBM	Conduction Band Minimum
CNL	Charge Neutrality Level
CTA	Chemical Technologies and Analytics
DFT	Density Functional Theory
DOS	Density Of States
EDS/EDX	Energy-Dispersive X-ray Spectroscopy
EPMA	Electron Probe Microanalyzer
GGA	Generalized Gradient Approximations
ICP-MS	Inductively coupled plasma mass spectrometry
ITO	Indium Tin Oxide
LDA	Local-Density Approximation
LDOS	Local Density Of Electronic States
LEED	Low-Energy Electron Diffraction
LEIS	Low-Energy Ion Scattering
NEXAFS	Near Edge X-ray Absorption Fine Structure

OLED	Organic Light Emitting Diode
OPA	Oxygen Plasma
OPVC	Organic Photovoltaic Cells
ORNL	Oak Ridge National Laboratory
PAMBE	Plasma-Assisted Molecular Beam Epitaxy
PES	Photoelectron Spectroscopy
SEM	Scanning Electron Microscope
STM	Scanning Tunneling Microscope
STS	Scanning Tunneling Spectroscopy
TCO	Transparent Conducting Oxide
UHV	Ultra-High Vacuum
UPS	Ultraviolet Photoelectron Spectroscopy
VBM	Valence Band Maximum
XPS	X-ray Photoelectron Spectroscopy
XRD	X-Ray Diffraction
YSZ	Yttria-Stabilized Zirconia

1. Indium Oxide

1.1. Introduction

Indium oxide, In_2O_3, has drawn increased attention from researchers over recent years. When doped with SnO_2, the material is commonly referred to as Indium Tin Oxide (ITO), which is the prototypical Transparent Conducting Oxide (TCO). ITO combines high optical transparency in the visible range with conductivity approaching that of a metal [1]. As a consequence of its interesting physical and chemical characteristics, it is widely used in several technical applications including transparent films for organic Light Emitting Diodes (OLEDS) and Organic Photovoltaic Cells (OPVC), gas sensing, and transparent infrared reflectors. In_2O_3 is also used in heterogeneous catalysis [2] and in chemical gas sensing [3]. Despite its technological importance, surprisingly little is known about the fundamental surface properties of ITO or those of pure In_2O_3. Even basic material characteristics, such as the fundamental band gap have been controversially discussed [4, 5]. The use of a value of 3.75 eV [6] for In_2O_3 (which is the optically-determined band gap) instead of the actual value of around 2.9 eV [4] has led to many incorrect conclusions especially regarding band bending and defect chemistry. Another problem of previous investigations was that the samples were mostly produced by magnetron sputtering, evaporation, or by pressing pellets of powder, which usually leads to polycrystalline, highly defective samples [7]. Much new information could be gained from epitaxially-grown In_2O_3 and ITO thin films [4, 8–10]. In the present work, high-quality, (001)-oriented single crystals are being examined. The availability of these crystals, in combination with a recent Density Functional Theory (DFT) work [11] that describes possible terminations of low-index In_2O_3 surfaces, was the motivation to undertake the present diploma thesis. The most important findings of this work will be published in Physical Review B in near future. Optical and resistivity measurements can be found in the preceding project work [12].

1.2. Crystal Structure

In_2O_3 can exist in three different modifications. In this work, only samples crystallized in the bixbyite structure (space group $Ia\bar{3}$) are considered (at higher temperatures and pressures perovskite or corundum structures can be observed [13]) . The bixbyite structure can be derived from a 2×2×2 fluorite lattice [14]. To obtain the bixbyite structure, 12 oxygen atoms per unit cell are removed from the anion sublattice in a systematic way. Each {001} anion layer contains four of these vacant oxygen positions. The cubic unit cell of In_2O_3 has – according to literature [15] – a lattice parameter of 10.117 Å (for a revised value see Section 3.4.2) and consists of 80 atoms: 32 indium atoms and 48 oxygen atoms (Figure 1.1). Two distinct indium positions can be found in the crystal, which have a different symmetry (Figure 1.2). These are commonly referred to as In-b (8 atoms) and In-d (24 atoms). The In-b sites are more regularly coordinated than the In-d sites. Along the (001) direction the crystal can be thought of as a stacking of three different layers. These can be identified as a mixed layer, which consists of In-b and In-d atoms (M-layer), a layer which contains only In-d atoms (D-layer), and an oxygen layer.

An important characteristic of $In_2O_3(001)$ is the polarity of its surface (Tasker type-III) [16, 17]: The alternating indium and oxygen layers lead to a net dipole moment perpendicular to the surface (independent whether the surface is indium or oxygen terminated). However, polar surfaces cannot have bulk-like surface terminations: in this case the electrostatic potential would diverge for a macroscopic material. A depolarization field is, therefore, required to stabilize the surface. This can be achieved by different mechanisms such as reducing of top and bottom layer surface charges, changes in surface stoichiometry, surface reconstructions, absorption, or faceting [17]. Recent Scanning Tunneling Microscope (STM) measurements of epitaxial ITO films showed that the non-polar (111) surface has a (1x1) structure with a simple bulk-like termination [8], while the polar (001) surface is considerably more complex [9]. These previous measurements were however complicated by the fact that (001)-oriented In_2O_3 films tend to facet, which leads to rough surfaces [10].

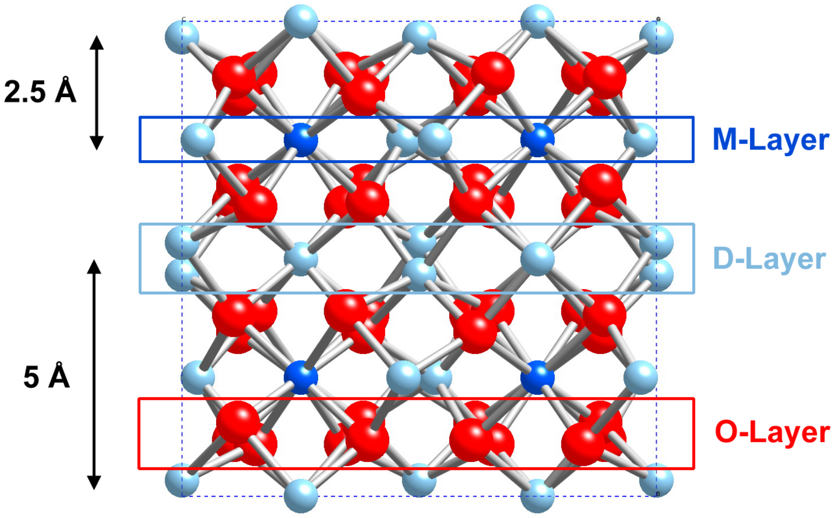

Figure 1.1.: In_2O_3 bixbyite structure. Red spheres indicate oxygen atoms, dark blue In-d, and light blue In-b atoms. Layers containing both types of indiums atoms (M-layer) are flat, in contrast to the layers that contain the In-d type only (D-layer).

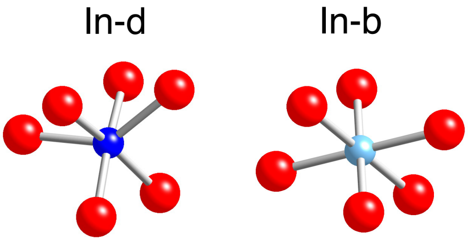

Figure 1.2.: The In-d and In-b sites.

1.3. DFT results for the terminations

As mentioned above, a recent DFT-based article from Agoston and Albe (VASP code, LDA, GGA-PBE) describes possible In_2O_3 terminations [11]. The authors found that for the stoichiometric crystals the surface energies increase with orientation in the order (111) < (011) < (211) < (001), which is in agreement with the results from [1]. It is surprising that the orientation with the highest surface energy is nevertheless often observed experimentally.

Both, stoichiometric (i.e., half of the indium/oxygen atoms missing from the bulk-terminated surfaces; see Figure 4.1) and non-stoichiometric surfaces were considered as a function of the oxygen chemical potential. For the stoichiometric surfaces these calculations show that the half oxygen terminations are energetically preferable compared to the half-indium terminations, again in agreement with previous DFT results from Walsh and Catlow [1]. The oxygen termination on top of the D-layer is favorable compared to an underlying M-layer. For the indium termination the M-layer is favorable. The differences are very small however. The resulting surfaces are shown in Figure 1.3. Due to the small energy differences between the different terminations Agoston and Albe conclude that considerable disorder has to be expected and that even a coexistence of different terminations could be possible.

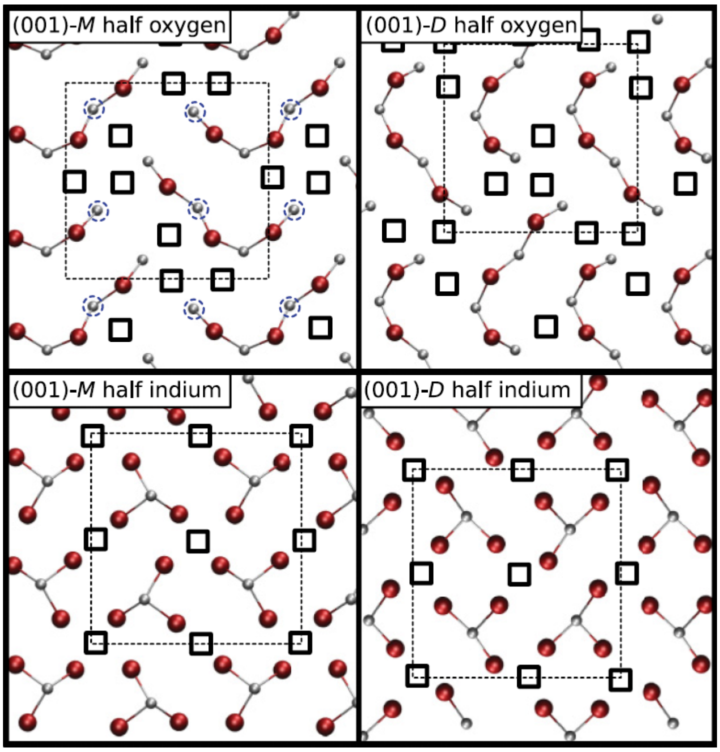

Figure 1.3.: Half oxygen and half indium termination for the M-layer and D-layer (Figure from Reference [11]). Missing lattice atoms are labeled by black boxes. In-b atoms are encircled in blue.

The surface stoichiometry depends on the oxygen chemical potential. The advantage of the oxygen chemical potential is that it can be easily converted into corresponding experimental environmental conditions [11]. Assuming an ideal gas the oxygen chemical potential μ_O at the temperature T and the pressure p is given by [18]

$$\mu(p,T) = \mu_O(p^0,T) + \frac{1}{2}kT\ln\left(\frac{p}{p^0}\right) \tag{1.1}$$

where $\mu_O(p^0,T)$ is the oxygen chemical potential at the investigated temperature T

and an arbitrary pressure p^0, and k the Boltzmann constant. $\mu_O(p^0, T)$ can be calculated from the tabulated enthalpy and entropy values of O_2 as described in Reference [18]. Equation 1.1 is however only unconditionally valid for equilibrium conditions.

Agoston and Albe found that different surface terminations become energetically preferable when going from highly reducing to highly oxidizing conditions in the following order:

- Additional indium nucleates on top of the surface
- Only 2 oxygen atoms per unit cell for the M-layer. 4 oxygen atoms per unit cell for the D-Layer
- Stoichiometric termination with six surface oxygen atoms
- Partial dimerized termination with two dimers and four oxygen atoms
- Dimerization of all oxygen atoms (i.e. peroxo species) for the M-layer. The fully dimerized D-layer would be strained for geometrical reasons and has therefore a higher surface energy

A dimerized surface would be in agreement with other DFT calculations, which predict that surface oxygen atoms undergo dimerization [3, 19]. The surface phase diagrams for the M- and D-layer can be found in Figure 1.4. The expected terminations for the metallic and the full peroxide surface can be found in Figure 1.5.

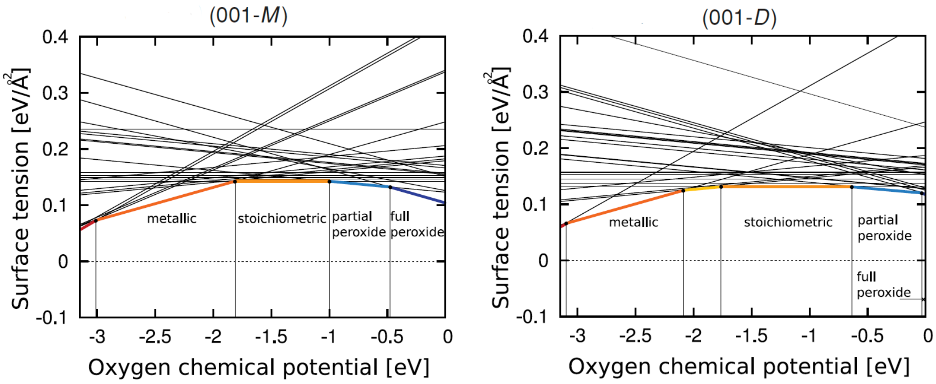

Figure 1.4.: Surface energy as a function of the oxygen chemical potential for the M- and D-layer from Reference [11].

Furthermore Agoston and Albe investigated the influence of water on the surface by calculating the surface energy as a function of different hydrogen chemical potentials.

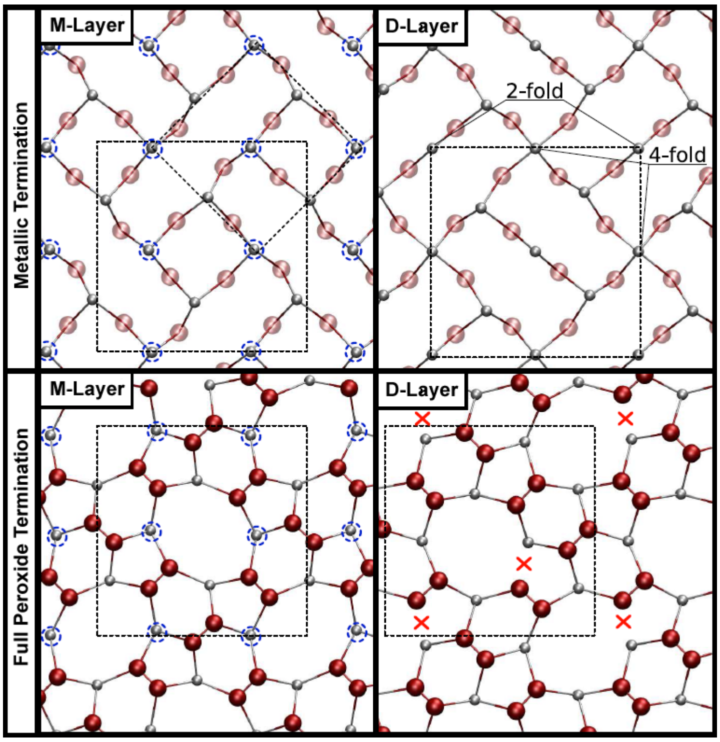

Figure 1.5.: Expected surface for the metallic and the peroxide termination from Reference [11].

The hydrogenated surface – which has 12 hydroxyls per unit cell – turns out to be the most stable one compared to all other (001) phases. For a complete removal of the water from the surface the chemical potential of the water has to be $\mu \geq 2.6$ eV which corresponds to about 580 K at Ultra-High Vacuum (UHV). Figure 1.6 shows simulated STM images for all terminations regarded in Reference [11].

1.4. Electronic Structure

1.4.1. Defect Chemistry

In_2O_3 is an n-type semiconductor. The n-type conduction arises from intrinsic donor defects, which also explains the pronounced non-stoichiometry observed under highly reducing conditions [20]. So far, In_2O_3 was regarded as a very good conductor even without extrinsic dopants due to its high carrier concentration [21]. The reason for the conductivity of undoped In_2O_3 has been discussed for a long time. De Wit first suggested that oxygen vacancies (V_O) are the dominating ionic defect [20]. Moreover a

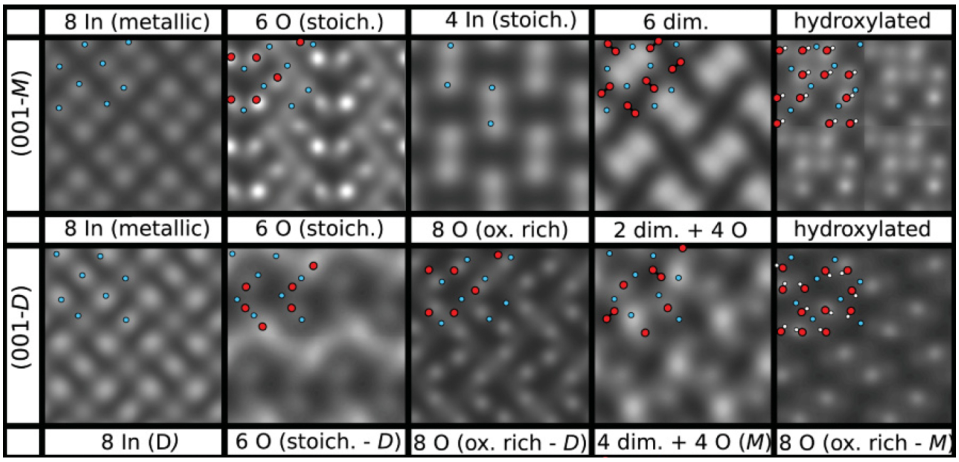

Figure 1.6.: Simulated STM image simulation of different $In_2O_3(001)$ terminations at a bias of +1.8 V (empty states) from Reference [11].

relation between the oxygen pressure and the conductivity has already been reported in the early years of the In_2O_3 investigations [13, 20, 22–24]. On the other hand, Tomita et al. claimed that oxygen vacancies cannot act as a native donor, because the defect level would be too far away from the Conduction Band (CB) [25] (note: a band gap of 3.75 eV was assumed by the authors). They suggested that interstitial indium could generate a shallow donor level, close to the CB. Yet, a complex of an oxygen vacancy and an interstitial indium would be even shallower and therefore the dominating electron source for the CB [25]. Lany and Zunger calculated that oxygen vacancies are formed in concentrations up to the 10^{20} cm^{-3} range while indium interstitials stay below 10^7 cm^{-3} [26]. The room-temperature electron density stays however below 10^7 cm^{-3} because the oxygen vacancies have a very deep level (their results are again based on a too high band gap of 3.5 eV). At high temperatures, transitions from the deep donor level could be possible because of the pronounced temperature dependent band gap shrinkage [26]. They suggest that the n-type conductivity arises from photoexcitation of the deep oxygen vacancies, which creates a shallow, conductive state near the Conduction Band Minimum (CBM). Back transition would be hampered by an energy barrier. Ambient background illumination could be enough to constantly regenerate the conductive state, which has a large optical cross section for F^+ ($= V_O{}^+$). Medvedeva and Hettiarachchi come to a similar conclusion: neutral oxygen vacancies are located close to the Valence Band Maximum (VBM), resulting in a fully occupied, non-conducting state [27]. Ionization of the vacancy is required for a conducting behavior. In contrast Agoston and Albe report that all intrinsic donor defects (oxygen vacancies V_O, indium interstitials In and indium antisites In_O) have low formation energies, are shallow donors, and can therefore produce free electrons in the CB [21]. However, oxygen vacancies have a lower formation energy than the interstitial and antisite donors and should be consequently the main contributor to the conductivity. In oxidizing conditions neutral oxygen interstitials in a dumbbell conformation (dimers) are the dominant defect.

Results of the Project work revised

Due to the deeper understanding of the the defect chemistry some of the results of the project work [12] can be newly interpreted:

- A surprisingly low conductivity of $2 \pm 0.5 \times 10^5$ Ω cm was discovered. The low conductivity of the crystals argues for deep oxygen vacancy states and/or a lower number of oxygen vacancies in general.

- The irreversible color change to orange upon annealing to 600 °C in UHV can be explained by desorption of oxygen and the formation of additional oxygen vacancies similar to the same effect for ZnO described in Reference [28].

- Optical spectroscopy showed a strong temperature dependence of the band gap of 1.11 meV/K from 200 to 500 K [12]. Weiher determined a similar value of 1 meV/K [29]. This could partly explain the rising conductivity with increasing temperature as the defect states wander towards the CB.

1.4.2. Density of States and the Valence Band

In general, the VB of In_2O_3 is dominated by O 2p-derived states with a lower VB peak from In 5s [1, 17, 19, 30]. The CB is dominated by the In 5s states. Interesting results have been published regarding surface states:

Klein investigated the surface of reactively evaporated In_2O_3 films in situ by synchrotron-excited photoemission [31]. He observed gap states depending on the oxygen pressures while preparing the films. He describes increasing intensity of the gap states with decreasing pressure, which goes along with an increase of optical absorption. He concluded that these surface gap states have their origin in different stoichiometries.

Agoston and Albe calculated the electronic structure of the surface of the reduced, the stoichiometric, and the full peroxide termination (Figure 1.7) [11]. The reduced surface shows In 5s-derived, half-filled metallic gap states which should have an acceptor character and therefore cause an upward band bending. For the stoichiometric surface they predict

– similar to Walsh and Catlow [1] – a split-off feature from the O 2p states close to the VBM, which is caused by undercoordinated oxygen atoms. For the surface under oxidizing conditions, peroxide surface states appear in the band gap coming from the anti-bonding p—π orbitals of the dimers. Other distinctive features for this termination are the bonding p—σ orbitals at the bottom of the VB and a ≈ 5 eV splitting of the O 2s states of the dimers.

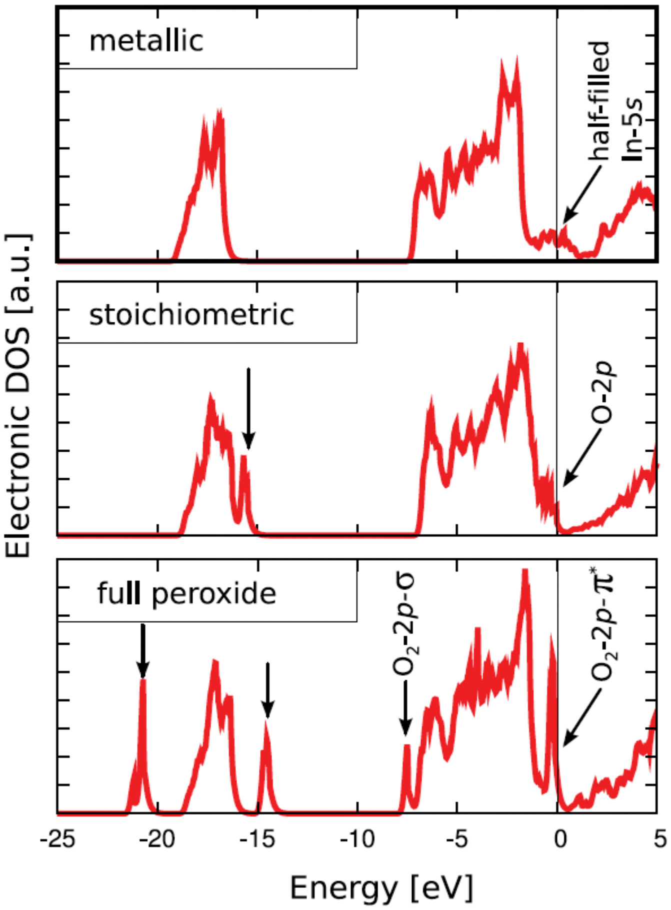

Figure 1.7.: Density of states for the metallic (reduced), stoichiometric and full peroxide termination from Reference [11].

1.5. Crystal Growth

The crystals were grown using a flux method [32] by Professor Lynn A. Boatner at Oak Ridge National Laboratory (ORNL), USA. The fluxes (solvents) used were B_2O_3 and PbO. In addition, a small amount of MgO was added. This mixture of In_2O_3, B_2O_3, PbO and MgO powders was melted in a platinum crucible and maintained at a temperature of 1200 °C for 4 to 10 hours. The temperature was then programmed to decrease by 3 °C per hour. As soon as a temperature of 500 °C was reached, the furnace was turned off. The crystals were extracted from the solidified flux using a 1:4 solution of nitride acid and water. The resulting cubic crystals are yellow-transparent and have side lengths between 1 and 2 mm as show in Figure 1.8.

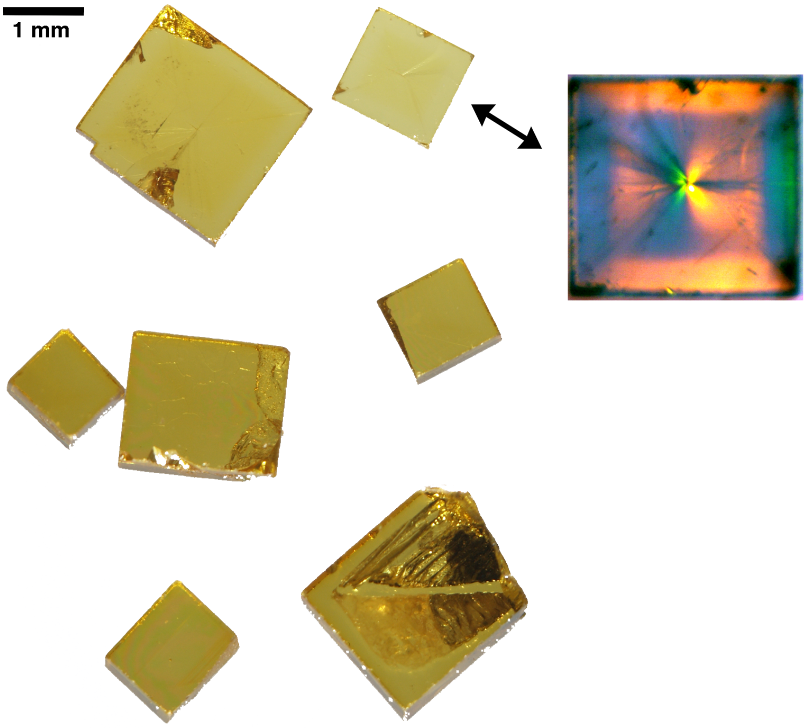

Figure 1.8.: The investigated $In_2O_3(100)$ single crystals. A polarized light microscope image of one of the crystal is shown.

2. Experimental Methods

2.1. Polarized Light Microscopy

Optical microscopy techniques that involve polarized light are called polarized light microscopy [33]. Polarized light is a contrast-enhancing technique, which can improve the quality of an image. The basic setup consists of a polarization filter (polarizer) positioned in the light path before the sample and a second polarization filter (analyzer) placed in the light path behind the sample. Usually a compensator (variable optical path length) or a retardation plate (fixed optical path difference) is mounted between the crossed polarizers, which is used to enhance optical path differences.

Materials with the same refractive index in all directions are called optical isotropic. All crystals of the cubic lattice system belong to this group. Crossed polarizes block the transmitted light through such materials completely and the image appears black.

Anisotropic materials are birefringent. The E-field oscillates in two perpendicular directions – the ordinary and the extraordinary polarization plane. In other directions the light does not remain linearly polarized. If the linear polarization is parallel to one of the two planes its direction is not changed and the light is blocked by the analyzer similar to an isotropic material. If the direction of the incident light is rotated against the two oscillation directions of the material, the light rays are split up into two components. They have different velocities and become out of phase depending on the strength of the birefringence and the thickness of the material. They are recombined with constructive and destructive interference when they pass through the analyzer. The optical path difference depends on the wavelength of the incident light. If white light is used, not all wavelength are influenced in the same way, which results in the extinction or amplification of certain colors. Materials that are usually isotropic can become anisotropic under strain and show birefringence.

2.2. Electron Probe Microanalyzer

The electron probe microanalyzer (EPMA) is a technique used for elemental analysis and chemical characterization of materials [34]. The specimen is bombarded with high-energy electrons (10-30 keV), which can create X-rays (characteristic X-rays and bremsstrahlung), electrons (secondary electrons, backscattered electrons, Auger electrons, photoelectrons), cathodoluminescence, and a specimen current. Characteristic X-rays are unique for each element, allowing its identification (however, sometimes peaks are overlapping). A subdiscipline of EPMA is the Energy-Dispersive X-ray Spectroscopy (EDS or EDX). The EDX spectrum shows the intensity of the characteristic X-rays – which is measured by a detector – as a function of the photon energy. The background is caused by bremsstrahlung. EDX cannot detect elements with a atomic number less than 4. Generally, the detection threshold gets worse for lighter elements.

EPMA are usually found in combination with a Scanning Electron Microscope (SEM). SEMs image a sample by scanning it with a high-energy beam of electrons and measuring the created secondary electrons and/or backscattered electrons. Secondary electrons image the topography of the sample. They have a low energy of a few eV, which means they are coming from the near-surface region. Backscattered electrons have an energy of a some keV. The intensity mainly depends on the atomic number of the specimen. Heavier elements backscatter more electrons and appear therefore brighter.

2.3. X-Ray Diffraction

X-Ray Diffraction (XRD) is a technique applied to investigate crystallographic structures [35]. It is based on elastic scattering (Thomson scattering) of X-rays from ordered structures. The measurement of the directions and intensities of the diffracted X-rays (diffraction pattern) allows one to deduce the positions of the atoms in a material.

Powder XRD (based on the Debye-Scherrer method) is the most widely applied XRD technique. It is used for the characterizing of microcrystalline powders. The sample consists of fine grains of crystalline material, which are randomly orientated. The sample is irradiated with collimated, monochromatic X-rays. Constructive interference can be observed if Bragg's law ($2d \sin \vartheta = n\lambda$) is satisfied and the X-rays are diffracted. The scattered radiation is usually measured on a flat plate detector. The randomly orientated crystallites lead to concentric diffraction rings corresponding to the various d spacings in the crystal lattice as shown in Figure 2.1. It can be necessary to rotate the sample to achieve a true random orientation of the crystallites. The positions and the intensities of the peaks (rings) are used for identifying the underlying structure. The scattering angle in X-ray crystallography is always denoted as 2ϑ. The data are usually presented as a diffraction diagram: The diffracted intensity is shown as function of the scattering angle 2ϑ.

It is difficult to determine an unknown crystal structure only from powder diffraction data due to the overlapping of reflections. However, the crystal structures can be refined using the Rietveld method. A theoretical line profile is refined until it matches the measured profile applying the least squares method.

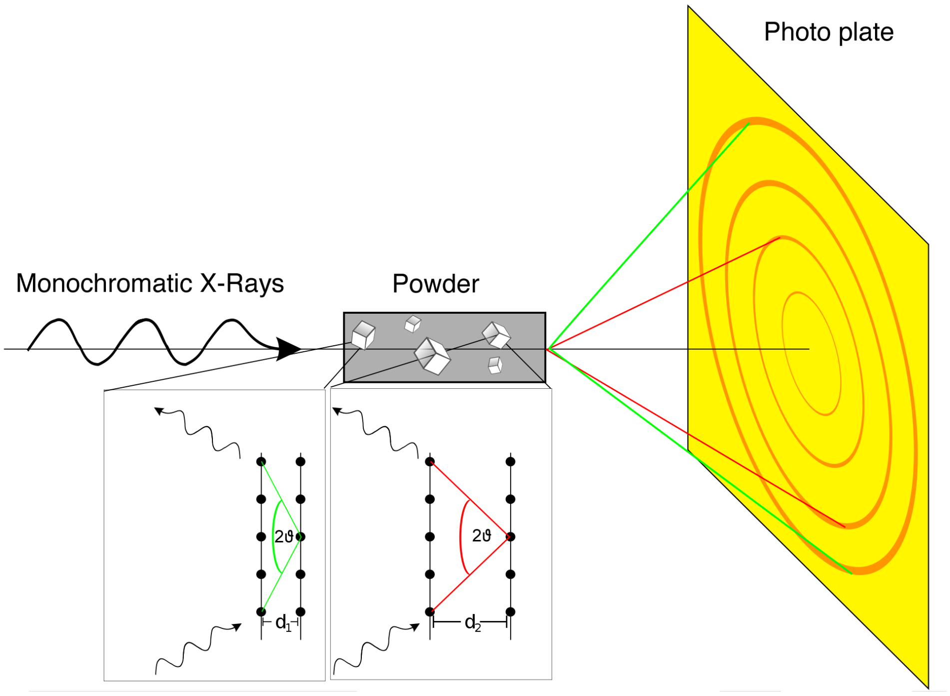

Figure 2.1.: Powder X-Ray Diffraction. Adapted from Wikipedia (Retrieved: September 13, 2011; http://de.wikipedia.org/wiki/Debye-Scherrer-Verfahren).

Single-crystal X-ray diffraction is used to solve the complete structure of single crystalline materials. The setup is similar to powder diffraction: A single crystal is irradiated with collimated, monochromatic X-rays. However, this time not rings, but discrete diffraction spots are observed as the single crystal lattice is (by definition) oriented the same way throughout the whole crystal. The angles and the strengths of these spots are recorded while the crystal is rotated by ϑ and the diffraction angle 2ϑ is varied simultaneously. The technique is so exact that not only the bond lengths but also the oscillation amplitudes of the atoms around their mean positions, the Debye Waller factor and the anisotropic vibrations can be determined with high precision.

2.4. Secondary Ion Mass Spectrometry

Secondary Ion Mass Spectrometry (SIMS) is a very sensitive surface analysis technique that allows the determination of the composition of solid surfaces [36]. It is able to detect elements in the parts per billion range. The surface of the specimen is sputtered with a high-energy ion beam (2 - 20 keV). The ejected secondary ions are collected and measured with a mass spectrometer. The method has many advantages:

- All elements can be measured
- High sensitivity
- Spatial resolution by scanning the surface with the focused ion beam
- Depth profiling is possible because material from the surface is sputtered away
- Vacuum in the 10^{-6} mbar is often sufficient (not for large molecules)

Few disadvantages speak against this technique:

- The sample is obviously destroyed by this method
- The quantification is difficult because the ionization probability depends on the chemical environment (matrix) and fragments of different elements can have the same m/q ratio due to multiple charged ions. Different chemical matrices have different sputter ion yields (SIMS matrix effect). As a consequence the ionic intensity does not vary linearly with the actual atomic composition of the sample [37]. For a quantitative measurement the relative sensitivity factors of the impurity species in the chemical matrix of interest are required.

2.5. Inductively Coupled Plasma Mass Spectrometry

Inductively coupled plasma mass spectrometry (ICP-MS) is a highly sensitive mass spectrometry technique for elemental analysis. The sample is ionized by an inductively coupled argon plasma [38, 39]. First, the sample material has to be transfered into the plasma. Liquid samples are converted into an aerosol by a nebulizer, which is then swept into the plasma. The transfer of material from a solid sample into the plasma can be achieved by laser ablation with a focussed laser beam (LA-ICP-MS). The ions are then analyzed with a mass spectrometer usually in combination with a quadrupole mass filter to separate the ions. A typical ICP-MS is able to detect elements in the part per billion (ppb) to part per trillion (ppt) range.

2.6. Scanning Tunneling Microscopy

STM is a widely used surface analysis technique developed by Gerd Binnig and Heinrich Rohrer at the IBM research laboratories in Rüschlikon from 1978 to 1981 [40, 41]. It revolutionized surface studies as it allows atomically-resolved imaging of conductive surfaces in real space.

The physics behind STM is based on the quantum mechanical tunneling effect. A small metal probe (usually an electrochemically etched tungsten tip) approaches a conducting sample to a distance of a few Å. Due to the tunneling effect electrons can overcome the vacuum barrier and can tunnel into unoccupied states of the sample or the tip before the STM tip contacts the sample (usual tip-to-sample-distances are around 0.5 - 1.5 nm). If no voltage is applied the tunneling would stop as soon as equilibration of the Fermi levels is reached. If a positive voltage is applied to the sample the electrons tunnel from the tip into unoccupied states of the sample. For a negative bias the electrons move from occupied sample states to the tip. The resulting tunneling current is amplified and recorded. The tip can be moved in all directions moved by a piezoelectric tube.

STMs are usually operated in constant current mode. This means that the tunneling current is kept constant by moving the tip closer or away from the surface while scanning. A feedback loop changes the tip-to-sample distance as soon as the tunneling current changes. Recording the tip-to-sample distance leads therefore to an image of the (electronic) topography of the surface. The experimental setup is shown in Figure 2.2. Under typical operation conditions tunneling currents are in the range between 0.1 and 10 nA and voltages vary from 1 mV to a couple of volts.

Theoretical Background

The basic principles of the tunneling process can be understood by applying the time separated one-dimensional Schrödinger equation on a rectangular potential $\phi = V - E$:

$$\left(-\frac{\hbar^2}{2m}\triangle + V\right)\psi(z) = E\psi(z). \tag{2.1}$$

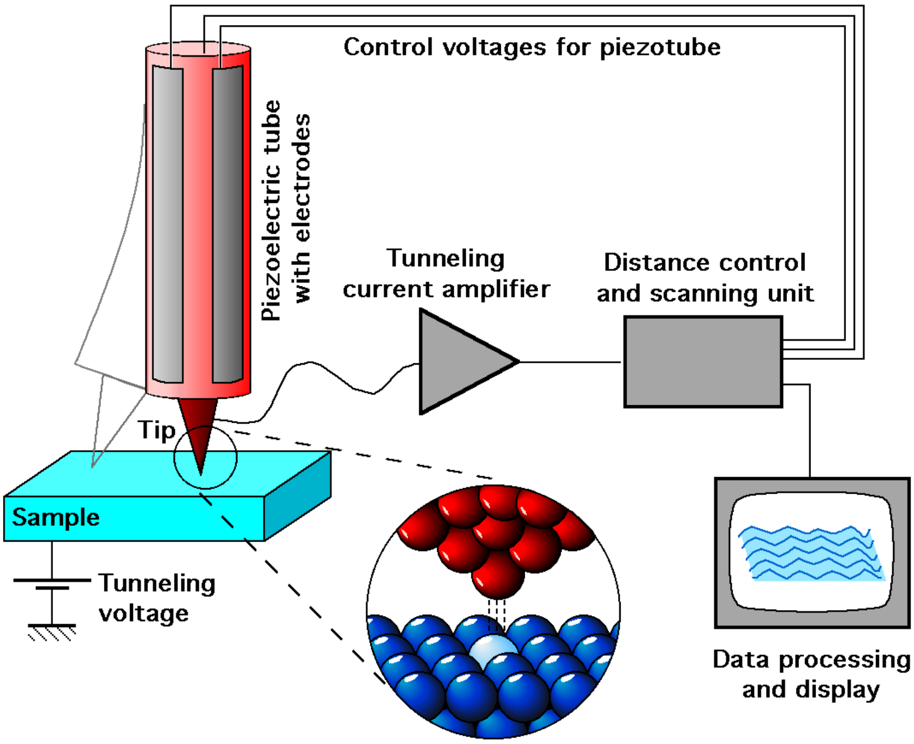

Figure 2.2.: Schematic of a scanning tunneling microscope from Wikipedia (Retrieved: September 13, 2011; http://en.wikipedia.org/wiki/Scanning_tunneling_microscope).

V is the vacuum barrier, ψ the wave function and E the electron energy. The solution of this equation shows an exponentially decreasing behavior within the vacuum barrier:

$$\psi(z) \propto e^{-\kappa z} \tag{2.2}$$

with

$$\kappa = \sqrt{\frac{2m\phi}{\hbar^2}} \tag{2.3}$$

The probability of an electron being at a position z within the barrier is proportional to $|\psi(z)|^2$. Assuming a barrier thickness of d the transmission probability T is then proportional to

$$T \propto |\psi(d)|^2 \propto e^{-2\kappa d}. \tag{2.4}$$

The tunneling current is proportional to the transmission. It therefore depends exponentially on the tip-sample distance. This allows to reach a very high resolution of

1/100 Å in the z-direction. The lateral resolution is however restricted to about ≈1/10 Å (see below). Furthermore the tunneling current depends on the density of states at the Fermi level and the applied voltage.

More sophisticated calculations were applied by Tersoff and Hamann [42] based on considerations of Bardeen [43]. They found out that in constant current mode the center of the spherical tip follows the contours of constant density of states of the sample surface. This means STM actually maps the electronic and not the true geometric structure. Furthermore the corrugation of the density of states decreases with increasing distance from the sample. This implies that the lateral resolution increases the closer the tip approaches the sample and the smaller the radius of the tip.

2.7. Scanning Tunneling Spectroscopy

Scanning Tunneling Spectroscopy (STS) is a technique which uses a STM to probe the Local Density Of Electronic States (LDOS) [36]. It allows the identification of surface states and the determination of the band gap. The tunneling current is measured depending on the voltage while keeping the distance constant (the feedback loop is switched off). The tunneling voltage is changed in small steps. At each step the tunneling current and the applied voltage – an I-V spectrum – are recorded. A schematic of the acquirement process can be found in Figure 2.3.

The tunneling current is proportional to the transmission probability, and the density of states of the sample ρ_s and the tip ρ_t. Assuming the tip behaves like a free-electron metal and has a constant density of states and a constant tunneling probability (which is only valid for low voltages), dI/dV becomes proportional to the density of states of the sample:

$$\frac{dI}{dV} \propto \rho_s(E_f - eU) \tag{2.5}$$

A positive bias samples unoccupied states whereas a negative sample measures occupied states. Usually the logarithmic derivative is used because it is less influenced by the transmission probability. To acquire an STM image and the I-V curves at the same time an AC modulation voltage is applied to the DC tip-sample bias. The AC component of the current in-phase with the modulation voltage is recorded with a lock-in amplifier.

In general it is very difficult to measure reproducible STS data. The tip has to be positioned at a constant height (within 0.01 Å) above the surface while the spectrum is taken. The current is influenced even by small height deviations and tip or sample changes

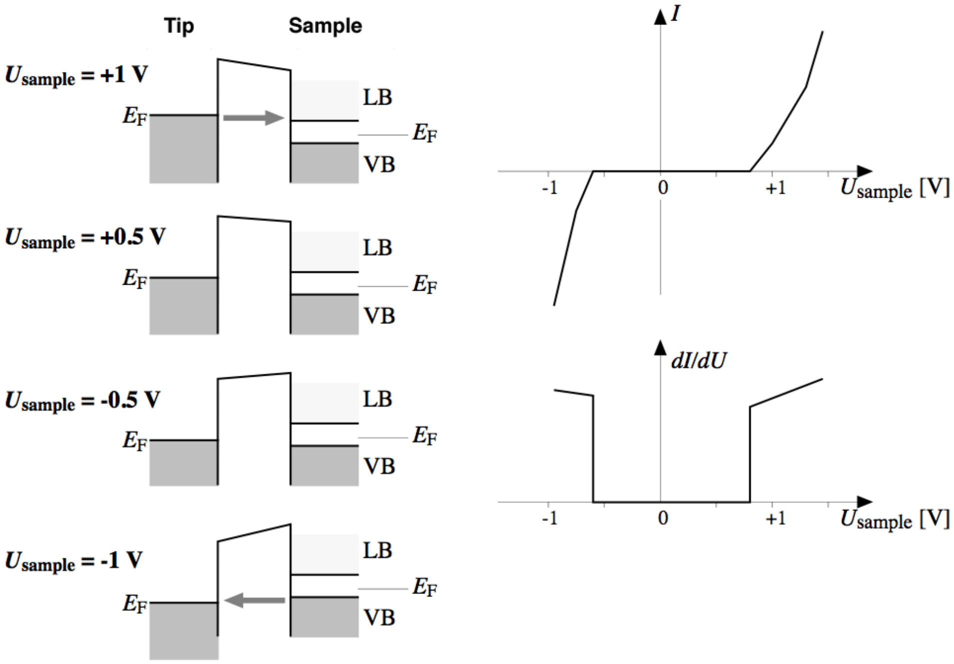

Figure 2.3.: Schematic of the acquirement of an I-V curve (Adapted from Reference [36]). Depending on the sample bias, electrons tunnel from the tip into the sample or vice versa. At the band gap no tunneling is observed provided that there are no gap states.

due to the applied voltage (the tip DOS is not constant). Therefore, it is necessary to take a STS spectra several times and average the spectra to obtain an acceptable signal-to-noise ratio. Another problem is that different tips will lead to different spectral features.

2.8. Photoelectron Spectroscopy

Photoelectron Spectroscopy (PES) refers to the measurement of the energy of photoelectrons emitted from a sample due to the photoelectric effect [36]. The photon energy has to be high enough for the electrons to overcome the work function. The energy distribution corresponds to the density of states. PES spectra usually show the binding energy with the zero-point at the Fermi energy. The binding energy (E_B) can be calculated from the conservation of energy by

$$E_B = h\nu - E_{\text{Kin}} - \phi \tag{2.6}$$

where $h\nu$ is the photon energy, E_{Kin} the kinetic energy of the electron and ϕ the work function of the detector.

Depending on the energy of the incident photons, two variants of PES can be distinguished: X-ray Photoelectron Spectroscopy (XPS) and Ultraviolet Photoelectron Spectroscopy (UPS). For XPS the photon energy is high enough to remove electrons from the core levels whereas UPS probes the valence band. Usually X-ray Kα radiation from magnesium or aluminum anodes is used for XPS. The radiation source for UPS are gas-discharge lamps. Alternatively synchrotrons can be used: They supply photons in a wide energy range, which allows the measurement of the valence band and the core levels at the same time.

The binding energy of the core levels depends on the chemical environment. Measurement of the chemical shift or core level shift therefore allows a chemical analysis. Even though X-rays can penetrate far into the bulk XPS is still a surface sensitive technique due to the small escape depth of photoelectrons. Sometimes it can be difficult to distinguish between XPS and Auger peaks. This problem can be solved by using X-rays with different wavelengths: the different photon energy will shift only the XPS peaks by the same amount but not the Auger peaks.

3. Experimental Results

3.1. Sample Preparation

A molybdenum sample plate and tantalum stripes were cleaned for ten minutes with acetone in an ultrasonic bath. Then these two parts were dried with CO_2 snow.

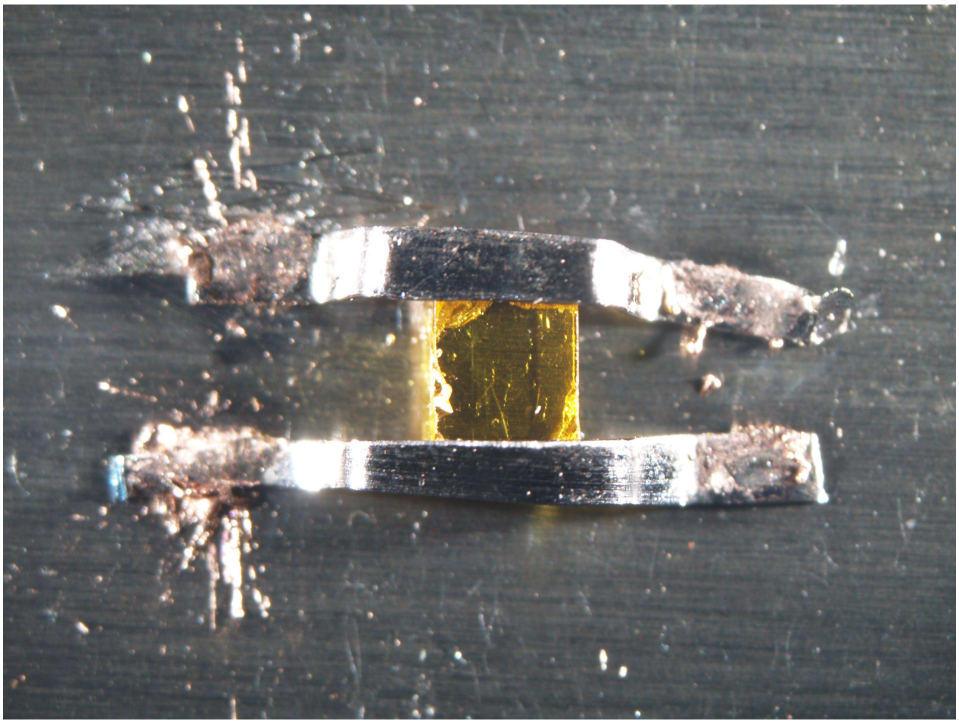

Figure 3.1.: Top view of an In_2O_3 single crystal mounted on a sample plate.

Afterwards the crystal was fixed with the tantalum stripes to the sample plate (Figure 3.1).

The initial sample preparation consisted of several sputter and annealing cycles in an UHV-chamber (base pressure $< 5 \times 10^{-10}$ mbar). A sputtering cycle included ten minutes surface bombardment with 2 keV argon ions (current density $\approx 10^{-5}$ A/cm^2). During the annealing excursions the sample was kept at a temperature of 500 °C for

10 minutes. After several sputter and annealing cycles the surface showed a sharp Low-Energy Electron Diffraction (LEED) pattern [12]. Auger Electron Spectroscopy (AES), XPS and Low-Energy Ion Scattering (LEIS) with 1 keV helium ions and a scattering angle of 105° confirmed that the surface is free of contamination [12]. LEIS, which is sensitive to strictly the top-most layer showed an indium peak that is far larger than the oxygen peak [12]. Annealing to higher temperatures (600°C) caused an irreversible color change of the crystal to orange, likely caused by the desorption of oxygen and the formation of additional oxygen vacancies, and was therefore avoided [12].

For the PES measurements the crystals where mounted on a rhodium crystal (Figure 3.2), which is described in more detail in Section 3.9.

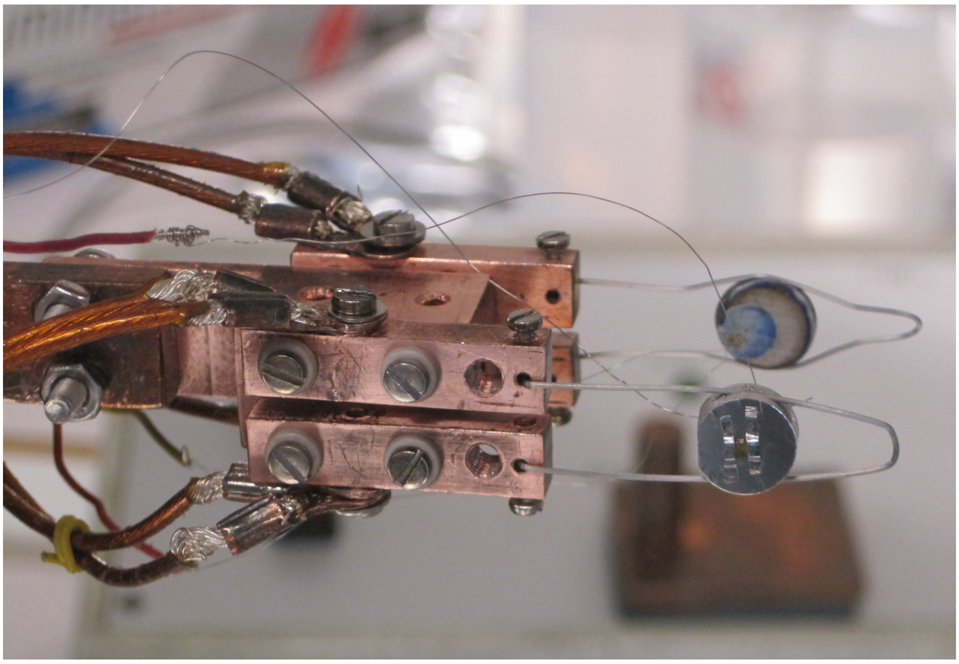

Figure 3.2.: A In_2O_3 single crystal mounted on a rhodium single crystal.

3.2. Polarized Light Microscopy

The polarized light measurements were performed in collaboration with Professor Kubel, Institute of Chemical Technologies and Analytics (CTA), TU Wien. Homogenous isotropic materials like the cubic In_2O_3 single crystals should not show birefringence. Figure 3.3 shows different images of one of the crystals taken with a polarized light microscope with a setup as described in Section 2.1. If one looks at the images in Figure 3.3 it is obvious that the crystal has to be birefringent as otherwise it would appear dark. As the cubic crystal lattice of In_2O_3 is not birefringent this result must be a consequence of stress in the crystal. the Figures 3.3 (a) and (c) show that the nucleation started from a single nucleus at the top of the crystal. The change from bright to dark areas in Figure 3.3 (b) after rotating the crystal 45 ° indicates different growth domains. In summary the polarization microscopy revealed that the crystals can be characterized as heterogeneous single crystals with multiple growth domains and stress birefringence.

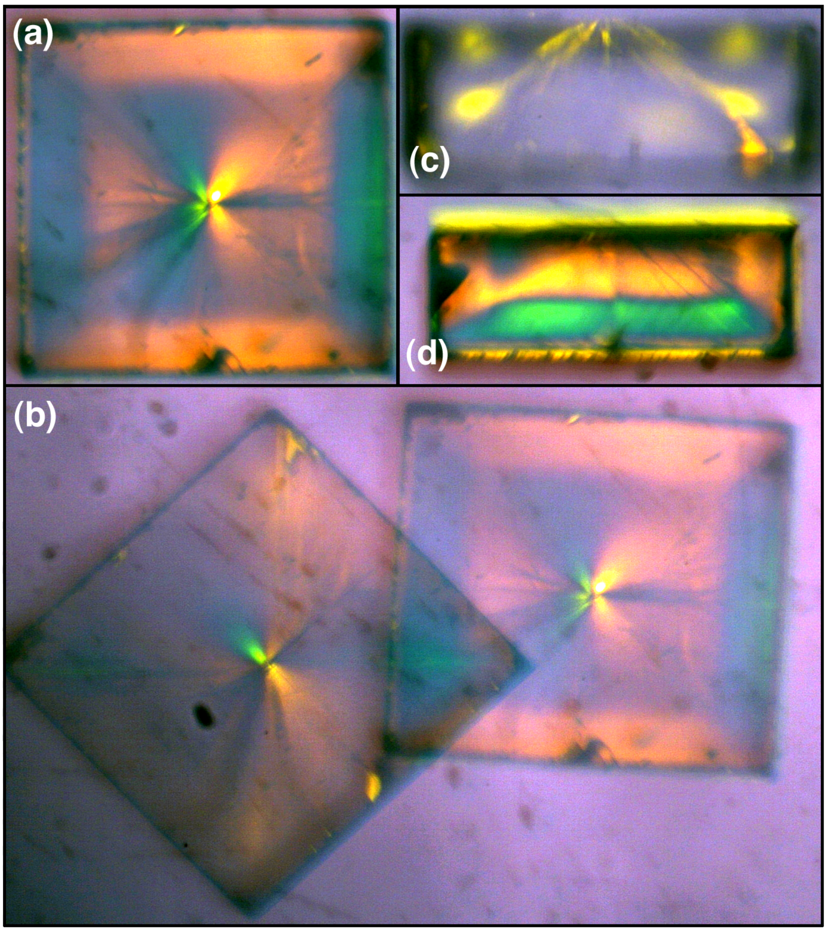

Figure 3.3.: Polarized light microscope images.

3.3. Electron Probe Microanalyzer

The purpose of the EPMA measurements was to determine which flux had been used for the crystal growth process. It was unknown whether a combination of PbO and B_2O_3 or

PbF_2 alone had been used. One of the crystals showed black spots on the surface. We suspected that these discolorations were residues from the flux. Furthermore it was an good opportunity to have a detailed look at the crystal surface with SEM. Figure 3.4 (a) shows a secondary electrons SEM image of the whole crystal whereas (b) shows a magnification of the top surface, where little craters are visible.

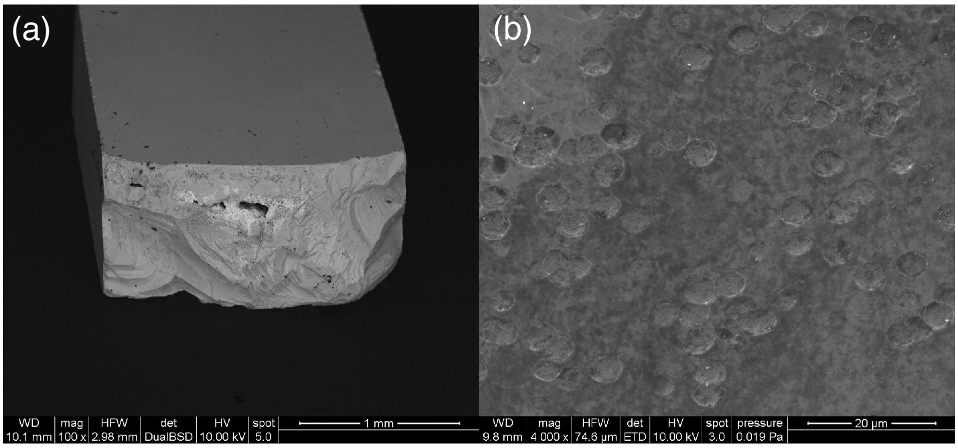

Figure 3.4.: (a) secondary electrons SEM image of the crystal. (b) shows a magnification of the top surface. The measurement parameters can be seen in the bottom of the images.

Figure 3.5 (a) shows a magnified backscattered electrons SEM image of the area where the dark spots are located. The bright areas seemed to be a promising position for the EDAX measurements since heavier elements (in this case the suspected lead) backscatter more electrons and appear brighter. EDAX spectra were acquired at three different positions indicated in Figure 3.5 (b): the flat surface (spectrum 1), at a protrusion (spectrum 2) and at the bright areas from the backscattered image (spectrum 3). Figure 3.6 shows the respective spectra. Spectra 1 and 2 look very similar: There are small indium, boron and lead peaks and relatively large oxygen and carbon peaks. The fluorine peak cannot be distinguished from the background. In contrast spectrum 3 shows a very strong lead peak and a stronger boron peak. The oxygen peak does not change in intensity. However, the indium peak has almost disappeared. The results of the three spectra together show that there are residues of the fluxes PbO and B_2O_3 on the surface. The relatively small boron peak can be explained by fact that EDAX has a lower sensitivity for light elements. The reason for the small indium peak compared to the oxygen peak in spectra 1 and 2 is not clear. It is possible that it can be attributed to the cross sections. The experimental setup has been provided by Professor Hutter, Institute of CTA, TU Wien.

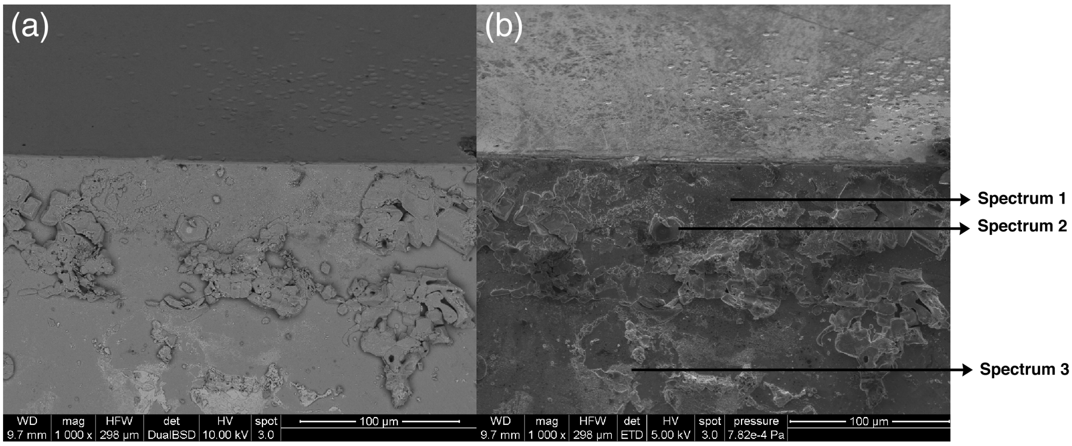

Figure 3.5.: SEM image of the crystal edge: (a) backscattered electrons; (b) secondary electrons. The measurement parameters can be seen in the bottom of the images.

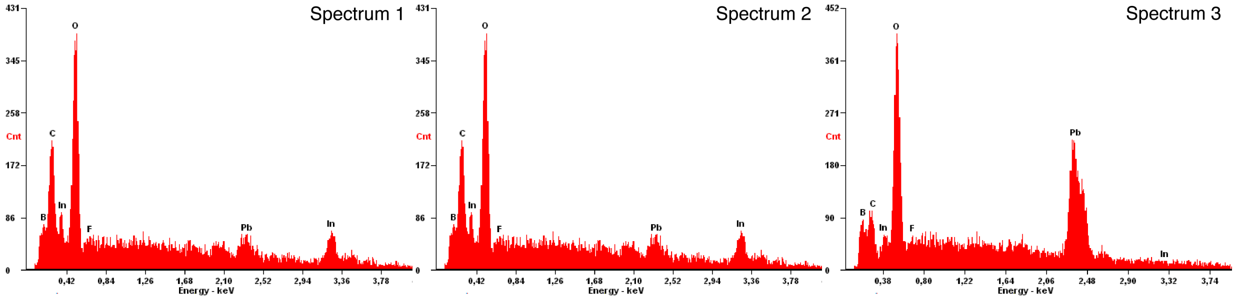

Figure 3.6.: EDAX spectra taken at three different positions.

3.4. X-Ray Diffraction

3.4.1. Powder X-ray Diffraction

In the beginning the main purpose to do powder XRD was to find an explanation for the strong temperature dependent color change [12]. A change of the crystal structure while annealing the crystal could explain this behavior. The measurements were again performed in collaboration with Professor Kubel. Off-the-shelf In_2O_3 powder from Sigma-Aldrich (99.999 %) was used for the measurements. The XRD measurement (coper Kα radiation; $\lambda = 1.5418$ Å) revealed a lattice constant of 10.12194(29) and an average crystallite size of 57.33(28) nm. Surprisingly, the spectrum (Figure 3.7) showed unexpected discrepancies from the expected results: A good fit could only be achieved by introducing heavy strain of 0.5148(31) % or assuming a tetragonal lattice instead of a cubic one. Furthermore the quantitive analysis revealed that the powder actually consists of 99.56898(85) % In_2O_3 and 0.43102(85) % pure indium metal.

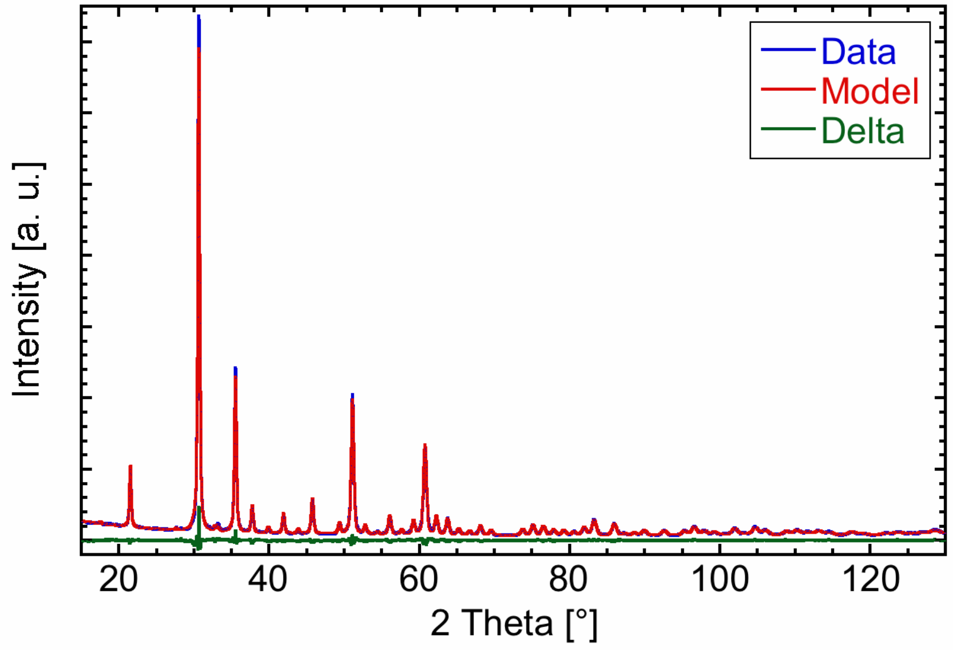

Figure 3.7.: XRD-spectrum of the untempered Sigma-Aldrich powder. The green line shows the difference between the data and the model.

A comprehensive literature research in the preceding project work showed that a temperature dependent band gap – which would explain the temperature dependent color change – is a normal behavior for many semiconductors [12]. Therefore the only open XRD question remaining was to explain the heavy strain of the investigated powder. Consequently the In_2O_3 powder was annealed to 500 °C for 30 minutes at ambient atmosphere. Purpose was to find out whether this procedure removes the strain. However, the new XRD measurements showed a lattice constant of 10.12052(28) Å, a crystallite size of 56.85(29) nm and a almost unchanged strain of 0.4933(31) %. Probably the powder was not annealed high enough to influence the strain. The XRD spectrum of the tempered powder can be found in Figure 3.8.

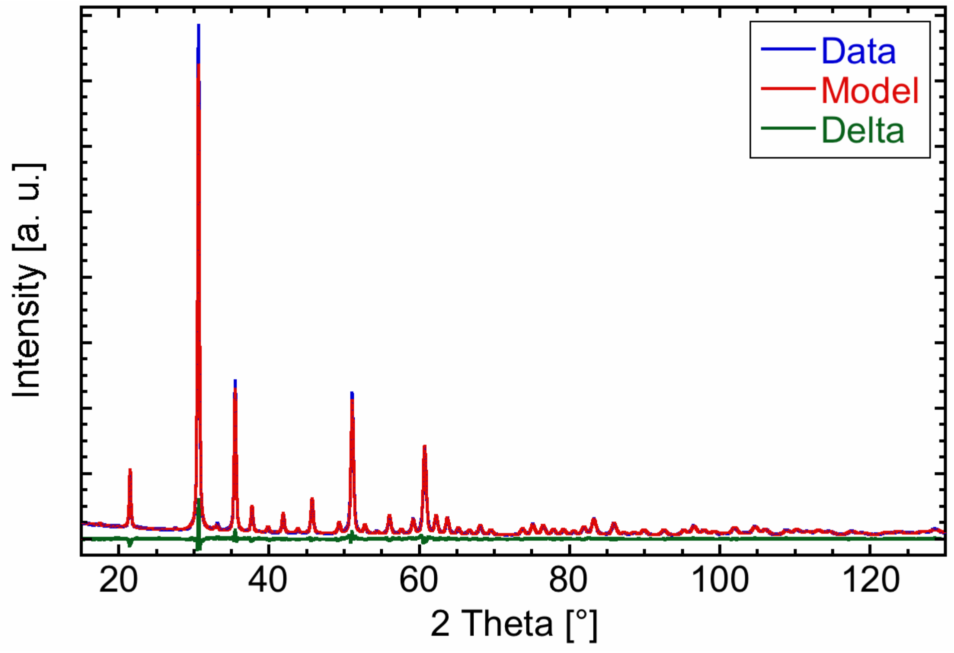

Figure 3.8.: XRD-spectrum of the tempered Sigma-Aldrich powder.

For comparison Figure 3.4.2 shows the XRD spectrum of a pulverized In_2O_3 single crystal. They come from a second batch of newly grown crystals, which have a black color. The results show that the crystallites are (unsurprisingly) larger compared to the powder samples and have a size of 333.9(86) nm. No strain was necessary to achieve a good fit. The lattice constant of this sample is 10.122768(91) Å.

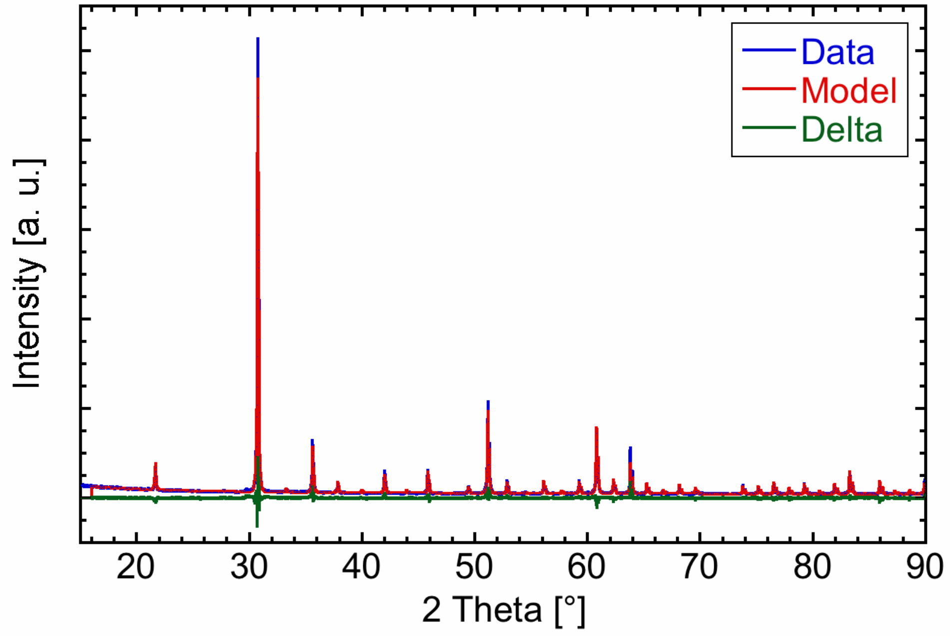

Figure 3.9.: XRD spectrum of a pulverized single crystals.

3.4.2. Single Crystal X-ray Diffraction

A small fragment broken from the corner region of the platelet was used for single crystal analysis. This crystal was controlled optically and showed no birefringence or domains. Structure analysis was made using a Bruker SMART diffractometer with a graphite monochromator and a SMART APEX detector using molybdenum Kα radiation ($\lambda = 0.71073$ Å) at room temperature (293 K). Frames were integrated using SAINT PLUS (Bruker, 2008) and absorption correction was performed using a multi-scan approach with SADABS (Bruker, 2008). The lattice parameters and systematic extinctions clearly indicate an orthorhombic space group $Ia\bar{3}$. The unit cell size was determined to 10.1150(5) Å. The structure analysis was made using the XTAL refinement package and converged to R=0.017 [44]. The atomic coordinates are given in Table 3.1. Details of the refinement are given in Table A.1, atomic displacement parameters can be found in Table A.2 and inter-atomic distances in Table A.3.

Site	Wyckoff Symbol	x	y	z	Occupation
In1	8b	0.25	0.25	0.25	1
In2	24d	0.466393(2)	0	0.25	1
O	48e	0.39037(2)	0.15470(2)	0.381852(19)	1

Table 3.1.: XRD: Atomic coordinates. Deposited at the Cambridge Crystallographic Data Centre. Deposition number CCDC 846726.

3.5. Secondary Ion Mass Spectrometry

The TOF-SIMS measurements were carried out on a TOFSIMS.5 (ION-TOF GmbH, Münster, Germany) instrument in collaboration with Prof. Hutter. Depth profiling was performed in the dual beam mode. The primary ions – produced by a liquid metal ion gun (LMIG) – were accelerated onto the sample, generating secondary ions, which were analyzed in a time-of-flight mass analyzer. A second beam from a Cs+ thermal ionization source (for negative secondary ion detection) eroded a crater on the sample surface during the flight time. An O_2^+ electron impact ionization source was used for crater erosion in positive secondary ion detection mode. As high mass resolution and good lateral resolution cannot be achieved with the same instrument settings, the primary ion beam for depth profiling was composed of short pulsed (<0.6 ns) Bi^+ ions for high mass resolution. An area of 500 × 500 μm^2 was sputtered while an area of 100 × 100 μm^2 was analyzed. The 700 scans performed correspond to a sputter depth of roughly 2200 nm. The depth profiles from SIMS for the most frequent elements in the crystals (Pb, Mg, Pt) showed a homogenous distribution (Figure 3.10) and no significant reduction of intensity with sputter time (Figure 3.11).

3.6. Inductively Coupled Plasma Mass Spectrometry

All measurements were carried out together with Dr. Limbeck (Institute of CTA, TU Wien). A NWR-213 laser ablation system from New Wave Research (ESI, Fremont, CA) coupled to a X-Series 2 ICP-MS System from Thermo Fisher Scientific (Bremen, Germany) was used. Instrument settings (see Table A.4) of the ICP-MS systems were optimized for maximum intensity while maintaining appropriate signal stability performing a line scan on a NIST 612 reference material. The laser settings used for optimization are given in Table A.5.

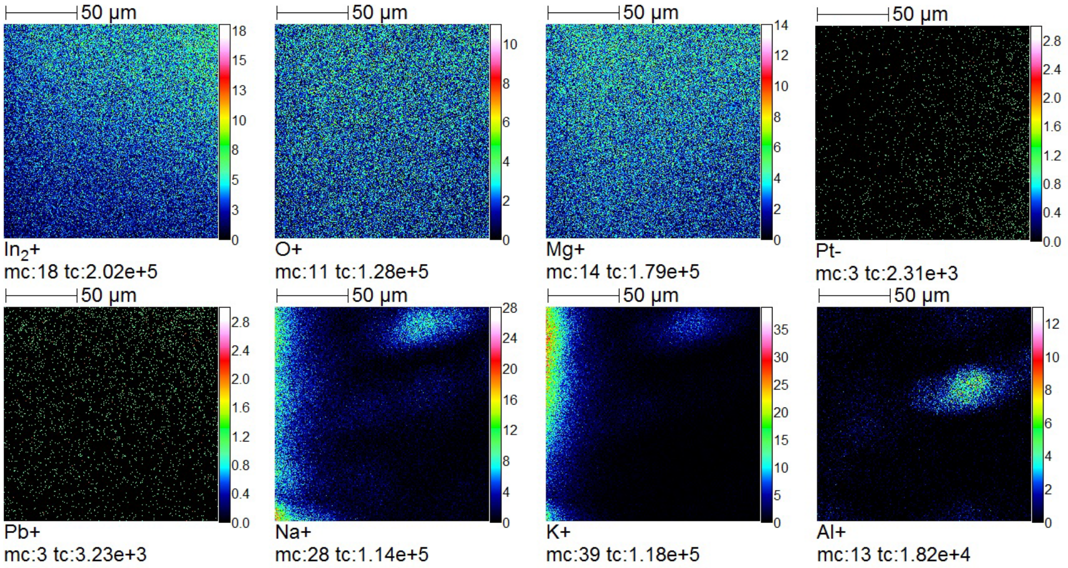

Figure 3.10.: Element distribution measured by SIMS.

For quantification purposes 2 different laser settings (50 % and 70 % laser energy) were used to investigate potential fractionation effects, which could not be observed, though. Each time nine different spots were ablated to minimize the influence of local irregularities of the sample. The trace impurities were quantified using a mass balance model based on the assumption that the target is 100 % In_2O_3 with a natural isotope distribution. For this purpose, instrumental mass bias was determined using the certified reference material NIST 612. Element concentrations were calculated from the acquired intensity counts with reference to the ^{113}In signal and the respective natural isotope abundance. Results were averaged from all 18 measurements and can be found in Table 3.2. Fluorine can not be ionized in an argon plasma due to its very high ionization energy. Therefore it can not be measured with ICP-MS. Traces of boron were found in the survey scans. The boron concentration was not measured quantitatively, though because of the low signal intensity and the fact that boron has generally a low detection limit with this technique. Its concentration can be estimate to 2 to 4 ppm.

3.7. Scanning Tunneling Microscopy

STM was performed in UHV (base pressure $< 5 \times 10^{-10}$ mbar) with two different instruments (SPECS Aarhus design and a customized Omicron micro-STM) using electrochemically etched tungsten tips at the surface science lab. Imaging was possible with

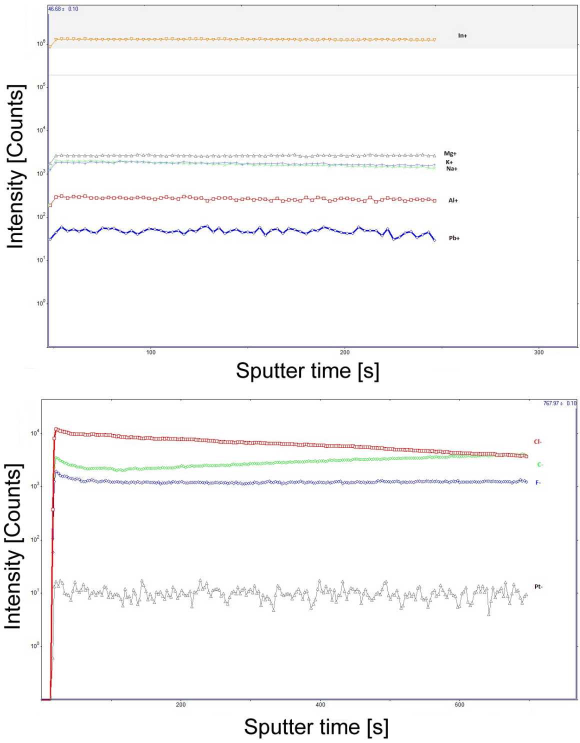

Figure 3.11.: SIMS depth profiles for the cations and anions.

both positive and negative bias with no apparent difference in the atomically-resolved images. A 100 × 100 nm^2 image of the sputtered/annealed (reduced) surface is shown in Figure 3.12. It exhibits wide terraces with relatively regular step edges. The line profile shows that the terraces have a step height of 5 Å. Figure 3.13 (a) shows a 20 × 15.75 nm^2 image with higher resolution. It is dominated by bright, atomic-sized protrusions, which, at the first sight, seem to be arranged in a disordered way. Analysis with Fourier transform, however, clearly reveals a square 3.6 Å lattice. This length equals a quarter of the diagonal of the In_2O_3 bulk unit cell. The lattice was obtained by creating a binary image with only one nonzero pixel at the center of each atom and extracting the 3.6-Å periodicity in the Fourier domain. The resulting lattice positions are shown as dots in Figure 3.13 (b). It is obvious that most atoms are close to a lattice site of this regular 3.6-Å grid, but not directly on it. Only a few atoms are far from lattice sites, sometimes close to the center of a grid cell. The coverage of the protrusions in Figure 3.13 amounts to about two per unit cell. The dark areas without protrusions are situated 2.5 Å below the protrusion level.

As shown in Section 1.3, the oxygen chemical potential has a strong influence on the termination. Therefore, the influence of exposing the surface to activated oxygen was

Element	Concentration [ppm]	SD
Pb	4307	± 74
Mg	1388	± 42
Pt	155	± 28
Nd	41	± 7
Zr	31	± 2
Sn	4.4	± 0.6
Sb	2.8	± 0.6
Bi	0.1	± 0.05

Table 3.2.: Concentrations and standard deviations of the elements found with ICP-MS.

investigated in the next step. As oxygen source an Oxford Scientific Oxygen Plasma (OPA) source was used. The oxygen pressure during the oxidation was usually around 5×10^{-6} mbar and the temperature 200 °C or 400 °C. First attempts were unsuccessful and led to a very rough and "dirty" surface. It turned out the the OPA source required further degassing before it could be used reasonably. Another problem was that the plasma could not be focussed very well on the sample and reacted therefore with adsorbates on the chamber walls. After 12 hours of degassing first promising images were taken. The same step height distribution was found, although the resulting surface appeared more complex in higher resolution images. Figure 3.14 shows a 100×100 nm^2 image of the oxidized surface. The large terraces, clearly visible on the reduced surface, are replaced by small islands. Generally, STM measurements at the oxidized surface were more difficult than at the reduced surface.

One of the results from Agoston and Albe was that water on the surface should lead to a hydrogenated surface, which has 12 hydroxyls per unit cell [11]. This hydrogenated surface should be the most stable one. Yet, dosing of 10, 20 and 100 Langmuir of water on the reduced or oxidized surface did not cause any obvious change. The results for the oxidized and the hydrogenated surface are, however, preliminary and further investigations are necessary.

An overview over all STM measurements as well as details for the preparation conditions are found in Table A.6.

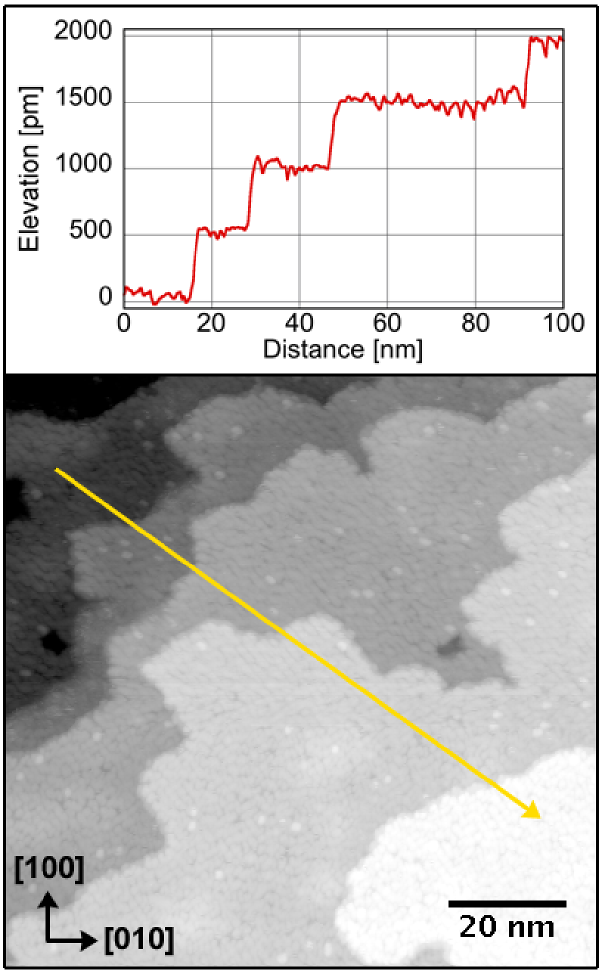

Figure 3.12.: STM image of a sputtered/annealed $In_2O_3(001)$ surface taken with a sample bias V_{Bias} = -3 V and tunneling current I_{Tunnel} = 0.225 nA. The arrow indicates the location of the line profile.

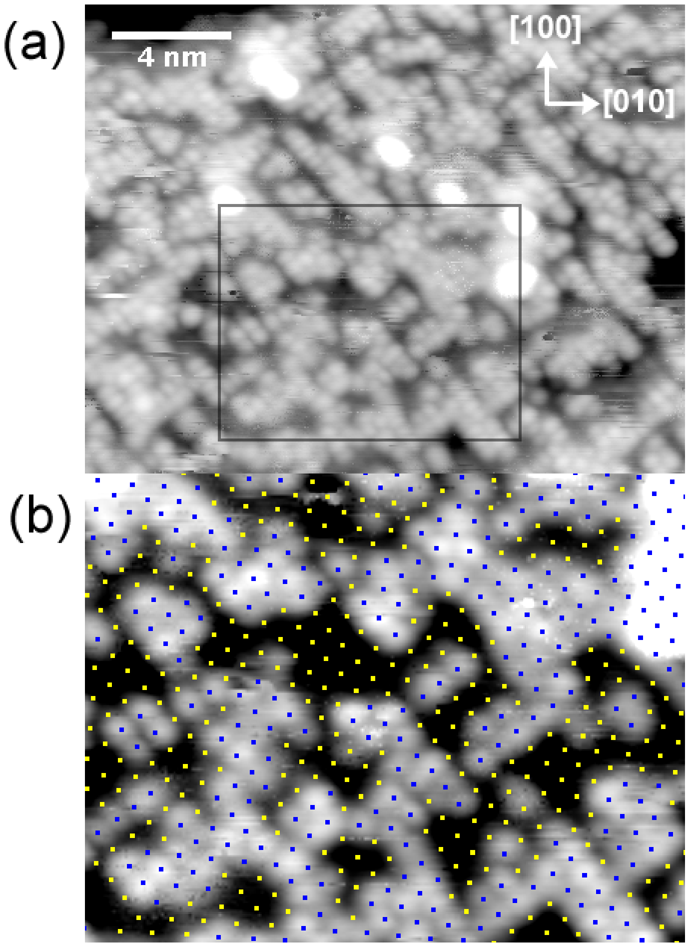

Figure 3.13.: (a) STM image with atomic resolution (V_{Bias} = -2.6 V, I_{Tunnel} = 0.17 nA). (b) This shows a magnification of the framed part above. The 3.6 Å lattice acquired from the Fourier transform is overlaid.

3.8. Scanning Tunneling Spectroscopy

STS was applied to measure the LDOS of the reduced sample around E_{F}. 400 spectroscopy points from a 20 × 20 grid in a 30 × 30 nm^2 area were acquired. A lock-in amplifier was used to directly obtain the differential conductance dI/dV, which is proportional to the LDOS. The voltage V_{BIAS} was modulated with 10 kHz and a voltage of 350 mV RMS. For each spectroscopy point dI/dV was measured in 50 steps from –1.19 V to +1.20 V. The STS spectrum in Figure 3.15 shows the average over the 400 dI/dV curves. A strong surface state at E_F is clearly visible.

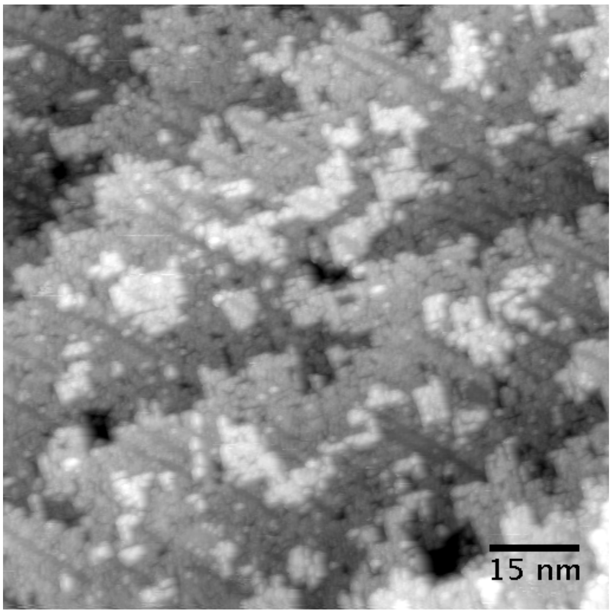

Figure 3.14.: STM image of the oxidized surface (100 x 100 nm^2, $V_{\text{Bias}} = 0.78$ V, $I_{\text{Tunnel}} = 0.42$ nA.

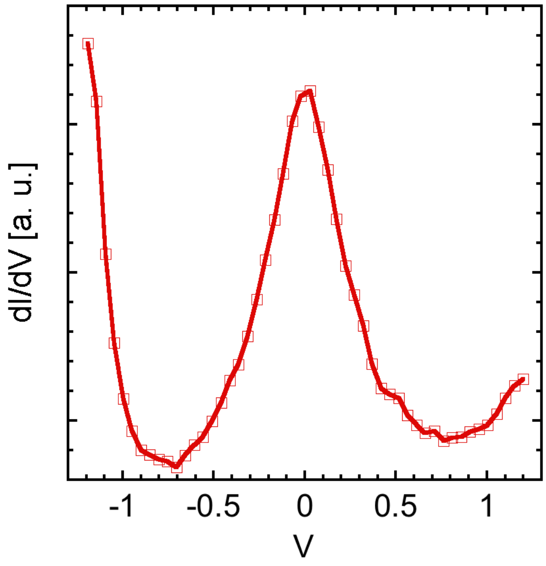

Figure 3.15.: STS of a sputtered/annealed $In_2O_3(001)$ surface.

3.9. Photoelectron Spectroscopy

High-resolution photoelectron spectroscopy was carried out at the MAX II storage ring at MAX-lab in Lund, Sweden in collaboration with Edvin Lundgren from Lund university.

The SX-700 monochromator at beamline I311 [45] supplies photons in the energy range from 43 to 1500 eV. The spectroscopy end station is used for high-resolution XPS and Near Edge X-ray Absorption Fine Structure (NEXAFS) measurements under UHV conditions (base pressure: $< 3 \times 10^{-10}$ mbar). The preparation chamber includes, among others, an argon ion sputter gun, LEED optics, mass spectrometer, and an atomic oxygen source (MBE-Komponenten OBS-40). A hemispherical energy analyzer (SCIENTA SES200) was used for the photoemission experiments. Measurements were performed at room temperature with the photon beam incident at 55° to the sample surface and normal emission. For the measurements the In_2O_3 crystal was mounted on a rhodium crystal (Figure 3.2), which allowed us to calibrate the Fermi energy by measuring the rhodium surface next to the In_2O_3 sample; it is defined as 0 eV binding energy for all of the spectra shown here. The Fermi energy had to be determined for each measurement as the indicated photon energies were imprecise. The reason for this is – among other things – inaccuracies of the alignment of the monochromator and differences between the injections of the electrons in the storage ring. The Fermi level was determined by fitting the Fermi edge with a Fermi–Dirac distribution. The results can be found in Table A.7.

All overview spectra were taken from 0 to 720 eV with a photon energy of 900 and 920 eV (Figures 3.16, 3.17). This allows the identification of the Auger peaks. The valence band region was acquired with photon energies of 60, 85, 105 and 185 eV as shown in Figure 3.18 (b). Due to the small size of the In_2O_3 crystals, it turned out to be difficult to completely avoid rhodium peaks. The rhodium counts could be minimized to about 1% of the In $3d_{5/2}$ counts, though. The Rh 4d-levels have a minimum in the cross-section for photoemission around 105 eV [46].

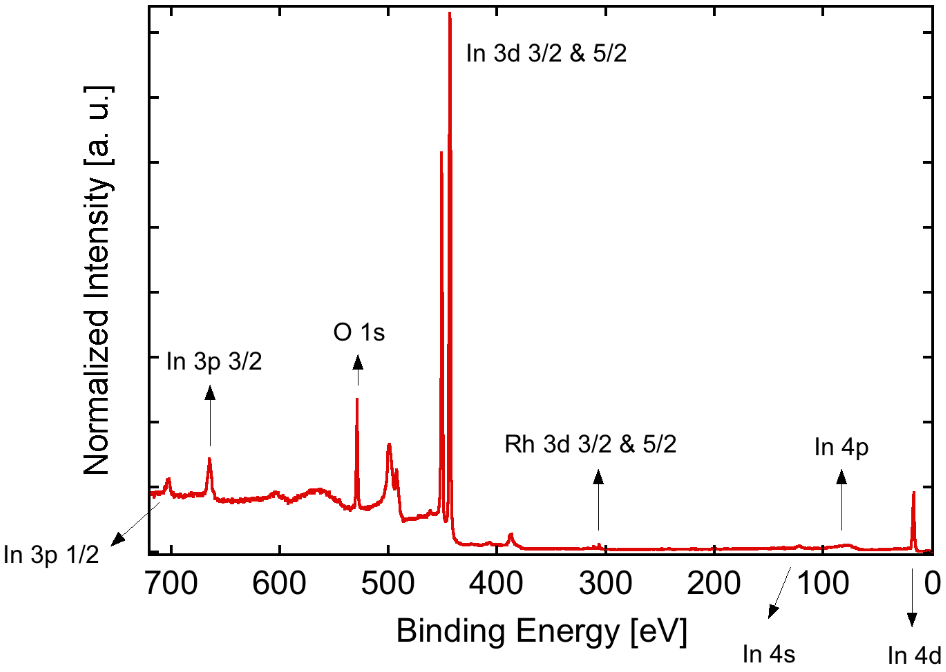

Figure 3.16.: Spectrum of the sputtered/annealed surface from 0 to 720 eV acquired at 900 eV photon energy. All photoelectron peaks are labeled.

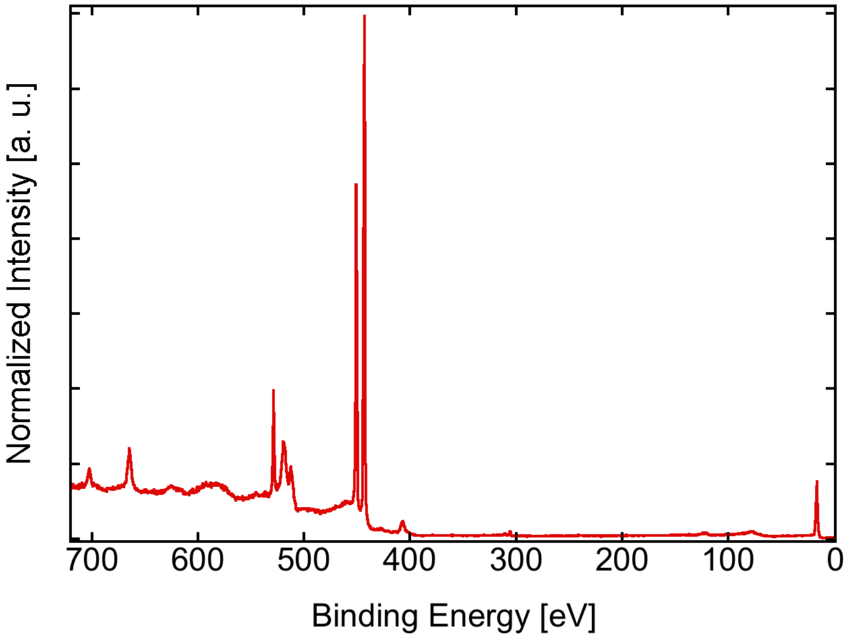

Figure 3.17.: Spectrum from 0 to 720 eV acquired at 920 eV photon energy. It can be seen that all unlabeled peaks from the previous figure have moved and are therefore identified as Auger peaks.

Sample preparation was identical to the one for STM. To oxidize the surface the crystal was treated with atomic oxygen for 30 minutes at an oxygen pressure of 3 × 10^{-7} mbar and a flux of ~ 5 × 10^{14} oxygen atoms cm^{-2} s^{-1}. While dosing, the sample was kept at a temperature of 200 °C or 400 °C. Figure 3.18 (a) shows a comparison of the VB of the reduced and the oxidized surface. The VBM is determined by extrapolating a linear fit of the leading edge of the valence band photoemission to the background level [47]. The VBM was determined using the data displayed in Figure 3.18 (a) and lies at 2.9 eV and 2.4 eV below E_F for the reduced and the oxidized surface, respectively. A shift of the same magnitude can be seen for the In $3d_{5/2}$ core levels (0.52 ± 0.11 eV, Figure 3.19 (a)) and the O 1s core level (0.54 ± 0.11 eV, Figure 3.19 (b)). The In 4d semicore levels are shifted by a smaller amount (≈ 0.3 eV). Probably they are influenced by the VB. The exact positions of the CL peaks was determined by fitting the data with a single curve using the software FitXPS, which uses a convolution of Gauss, Lorenz and Doniach-Sujnic line shapes (the convolution of the Gaussian and the Lorentzian profile is called Voigt profile) . The results of several measurements were averaged to get a more reliable value. Details can be found in the appendix (Table A.8 for the In $3d_{5/2}$ CL and Table A.9 for the O 1s CL).

A closer look at the O1s peak of the oxidized surface reveals a shoulder at the higher binding energy, shifted by 1.84 eV with respect to the main peak as shown in Figure 3.19 (c). The results from the line fits can be found in Table A.10. Further remarkable features in Figure 3.18 (a) are the pronounced gap states of the sputtered/annealed surface, which completely disappear for the oxidized surface. Figure 3.18 (b) shows the VB of the reduced surface at different photon energies. It is apparent that the intensity of the gap states decreases with increasing photon energy, i.e., with decreasing surface sensitivity.

Next, the indium-to-oxygen ratio change with surface sensitivity was investigated. The respective PES results were quantified by measuring the peak area of the In $3d_{5/2}$ and O 1s core levels for different photon energies (i.e. surface sensitivities). The area was determined in two different ways: (1) the peaks were fitted with FitXPS (Table 3.3); (2) the area under the peaks was manually calculated with KaleidaGraph after subtracting a linear background (Table 3.4).

The photoionization cross sections from Reference [46] (Table 3.5) were taken to correct the count rates. Surprisingly, the results show for both methods an increasing indium-to-oxygen ratio with increasing photon energy, which would contradict the assumed indium termination. Even more surprisingly, the indium-to-oxygen ratio is higher for

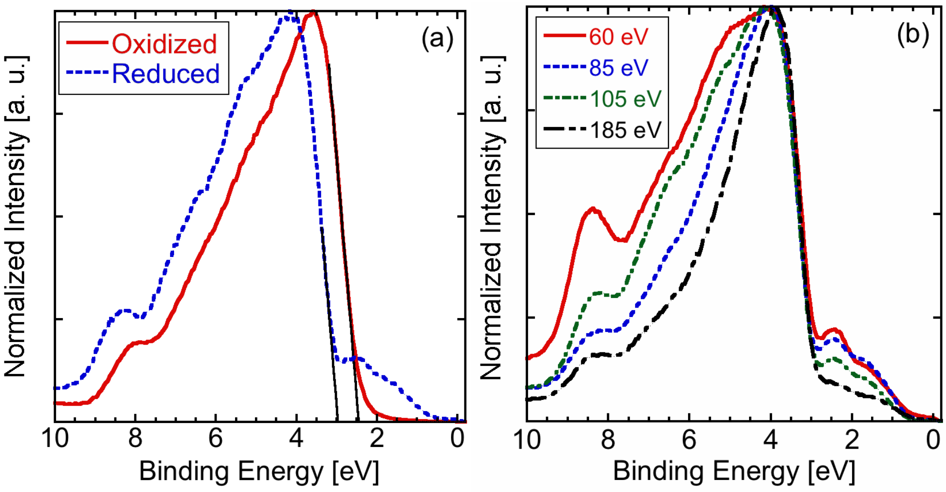

Figure 3.18.: (a) Normalized valence band spectra of the oxidized and reduced $In_2O_3(001)$ sample at 105 eV photon energy. Linear extrapolations for determining the leading edge of the VB are indicated. (b) The VB of the reduced surface at different photon energies.

the oxidized surface compared to the reduced surface. However, diffraction effects were neglected, which could have a strong influence on the peak area. The results from the peak area considerations should be, therefore, regarded with reservations.

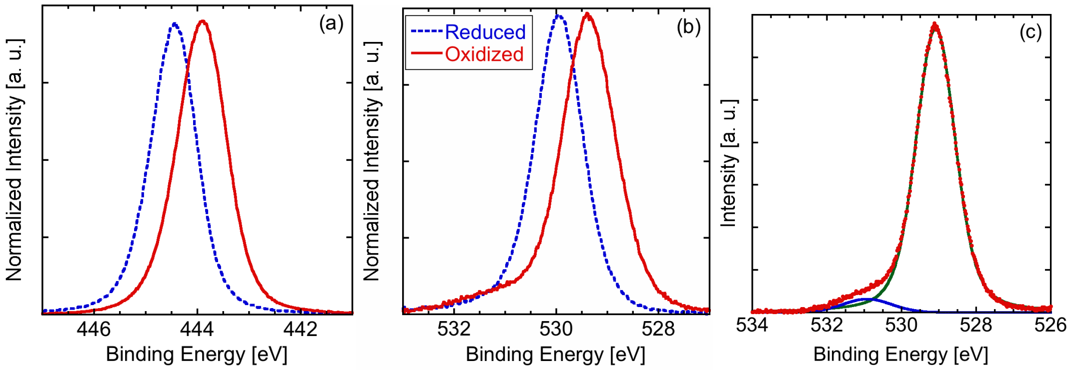

Figure 3.19.: PES of the (a) In $3d_{5/2}$ and (b) O 1s core levels, taken with a photon energy of 610 eV. (c) Line fits of the O 1s peak of the oxidized surface at 610 eV with the software FitXPS (c).

	Energy [eV]	#	In $3d_{5/2}$counts	#	O 1s counts	Ratio
Reduced	610	44	5.92E+03	46	3.62E+04	0.16
	660	62	2.55E+03	64	8.02E+03	0.32
	710	48	4.10E+03	50	1.14E+04	0.36
	760	65	3.19E+03	67	7.10E+03	0.45
	810	52	3.84E+03	55	8.57E+03	0.45
Oxidized	610	410	5.20E+03	412	2.06E+04	0.25
	660	430	3.20E+03	432	8.43E+03	0.38
	710	415	5.48E+03	417	1.36E+04	0.40
	760	433	4.68E+03	435	9.84E+03	0.48
	810	419	6.31E+03	421	1.44E+04	0.44

Table 3.3.: Change of the indium-to-oxygen ratio with increasing photon energy for the reduced and oxidized (at 400 °C) surface. The fitting was done with FitXPS.

	Energy [eV]	#	In $3d_{5/2}$ Counts	#	O 1s Counts	Ratio
Reduced	610	44	5.84E+03	46	3.67E+04	0.16
	660	62	2.56E+03	64	8.74E+03	0.29
	710	48	4.05E+03	50	1.19E+04	0.34
	760	65	3.19E+03	67	7.63E+03	0.42
	810	52	3.82E+03	55	9.13E+03	0.42
Oxidized	610	410	5.06E+03	412	2.12E+04	0.24
	660	430	3.12E+03	432	8.78E+03	0.36
	710	415	5.39E+03	417	1.38E+04	0.39
	760	433	4.58E+03	435	1.02E+04	0.45
	810	419	6.23E+03	421	1.44E+04	0.43

Table 3.4.: Change of the indium-to-oxygen ratio with increasing photon energy for the reduced and oxidized (at 400 °C) surface. The fitting was done by manually subtracting a linear background.

Energy [eV]	In $3d_{5/2}$ cross section [Mb]	O 1s cross section [Mb]
610	2.83	0.39
660	2.45	0.32
710	2.09	0.27
760	1.83	0.23
810	1.57	0.19

Table 3.5.: The photoionization cross sections for the required photon energies from Reference [46].

4. Discussion

4.1. Surface Structure

As shown in Figure 3.12 the step edges of the $In_2O_3(001)$ surface have a height of exclusively 5 Å. This has an important consequence if one regards the crystal structure of In_2O_3 (Figure 1.1): the distance between equivalent layers (e.g. from M- to M-layer) is roughly 5 Å. However, adjacent layers (i.e., from M- to D-layer) have a distance of about 2.5 Å. The observation of 5 Å-high steps implies that the large terraces have one particular termination, either M or D.

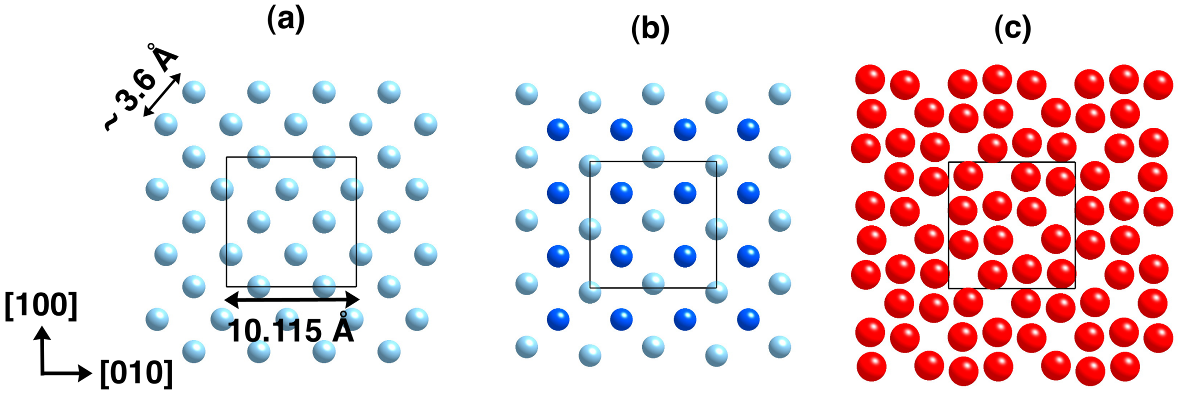

Figure 4.1.: Crystal models of the $In_2O_3(001)$ surfaces with (a) D-layer, (b) M-layer (b), and (c) O-layer termination. Shown are bulk-terminated layers with all the In and O atoms present. Note that these terminations represent polar surfaces; for stoichiometric surfaces only half of the atoms shown here are expected to be present.

In a recently published paper by Agoston and Albe [11] (summarized in Section 1.3) it was shown that the termination can vary strongly with the oxygen chemical potential. For the sputtered/annealed surface, we can safely rule out a (partial) peroxide termination for the following reasons:

- To prepare the sample it was annealed to 800 K in an oxygen background pressure of less than 1 × 10^{-12} mbar. The oxygen chemical potential $\mu_O(p^0, T)$ at 800 K and a pressure of 1 atm = 1013 mbar is according to Reference [18] -0.85 eV. Applying these values to equation 1.1 gives an oxygen chemical potential of -2.04 eV during the preparation. This should lead for the M-layer to a metallic termination according to Figure 1.4. However, this value is only a rough estimate as the required equilibrium conditions are not fulfilled.

- The top-layer consists predominantly of indium according to LEIS [12].
- According to simulated STM images dimers should appear dark [11].
- As suggested by Gassenbauer et al. [48], a surface peroxo species should show an O 1s core level with an additional structure at the higher binding energy side. While we indeed see such a peak for oxidized surface in Figure 3.19 (c), it is absent for the sputtered/annealed surface.

At first sight the atom-sized features in Figure 3.13 (a) seem to be arranged in an unsystematic way. As shown in Figure 3.13 (b), most protrusions (atoms) are close to lattice sites of a 3.6 Å lattice, rotated by 45° with respect to the axes of the unit cell. The ball model in Figure 4.1 (c) shows that all oxygen atoms are situated close to lattice sites of a square lattice with $a/4 \approx 2.5$ Å, aligned with the axes of the unit cells. We have examined whether the protrusions visible in the STM image (Figure 3.13) could fit to such a lattice, but we found no solution that is compatible with the fourfold symmetry of the surface. The arrangement of the indium atoms is a distorted 3.6 Å lattice rotated by 45°, for both, D- and M-terminations (see Figure 4.1 (a), (b)). This suggests that the protrusions visible in the STM image of the sputtered/annealed surface are indium atoms, but that this indium lattice is only partially occupied. The number of protrusions in the STM image is determined as two per unit cell; this corresponds to half the In atoms expected for a stoichiometric In-terminated surface (or 1/4 of the density of a full indium D- or M-layer shown in Figure 4.1 (a) and (b)). Comparing the atoms in Figure 3.13 with the simulated STM images for the reduced surface (Figure 1.6) the elongated shape of the atoms could be an indication that we see the D-layer. The unresolved dark areas in Figure 3.13 would then be the M-layer. The surface would thus consist of an M-layer at the basis, with small, irregular patches of a D-layer on top. Interestingly, the STM results obtained in this work show quite a different appearance compared to the ones obtained earlier by Morales and Diebold [9]. They investigated thin films of ITO(001) grown on Yttria-Stabilized Zirconia (YSZ), prepared with an oxygen plasma source, i.e. under highly oxidizing conditions. Protrusions arranged in a zig-zag pattern were observed and interpreted as oxygen dimers of the peroxide termination. Cross-shaped dark features were attributed to missing dimers. The samples investigated in Reference [9] differ in various ways from the single crystals studied here: They have been grown in a highly oxidizing environment, they consisted of relatively thin epitaxial films that may have been influenced by strain induced by the YSZ substrate, and they were doped with Sn. All three parameters are expected to affect the surface termination; although it needs to be left to a future investigation to what extent.

The quality of the STM images of the oxidized surface (Figure 3.14) are not good enough yet to make a conclusion regarding the termination from the STM data. However, the data from the PES measurements help us to understand the oxidized surface: The photoelectron spectrum of the O 1s CL of the oxidized surface (Figure 3.19 8 (c)) shows a shoulder attributed to the presence of peroxide species. Agoston and Albe [11] considered a ‘full’ peroxide termination (6 dimers/unit cell) and the ‘partial’ peroxide surface (2 dimers, 4 oxygen atoms). Assuming we probed three monolayers with PES (due to the photoelectron escape length at a kinetic energy of ~100 eV), the expected ratio of oxygen in peroxide versus oxygen in bulk-like positions should be ~1/3 and ~1/10 for the full and partial peroxide termination, respectively. The intensity ratio of the shoulder to the main O1s peak in 3.19 (c) amounts to 5.3%. This indicates that the oxidized crystal has a considerably lower peroxide coverage than the full peroxide termination.

4.2. Electronic Structure

4.2.1. Bulk Properties

Initially, the results from the four-point-probe measurements from the project work [12] will be discussed. The accuracy of the resistivity values is limited by the fact that no distinction between bulk and surface conductivity is possible. Also surface states may play a role in the surface conductivity. This makes it difficult to determine the resistivity accurately, but they do give an order of magnitude that will be sufficient for the following considerations. The carrier concentration n can be calculated from the conductivity σ and the carrier mobility μ using the relation [49]:

$$n = \frac{\sigma}{e\mu} \tag{4.1}$$

The conductivity $\sigma = (5 \pm 1.3) \times 10^{-6}\ \Omega^{-1}\ \mathrm{cm}^{-1}$ was calculated from the room temperature value from the resistivity measurements after a temperature excursion to

500 °C (probably the most reliable value). The carrier mobility value $\mu = 32$ cm^2 V^{-1} s^{-1} was obtained from Reference [4]. The carrier concentration then results in $(1 \pm 0.2) \times 10^{12}$ cm^{-3}, which is about seven magnitudes smaller than the lowest value reported in literature (see Reference [4]). This means that our crystals have fewer impurities than the ones investigated in previous publications. This is emphasized by the fact that our crystals are yellow compared to the often reported green or black coloration [13]. A possible reason for this extremely low carrier concentration might be the Pb and Mg residues in the crystals: they could compensate the natural n-type doping by a p-type doping.

Nevertheless this value is probably still assessed to be too high, and it gives an upper limit for two reasons. First, absorbed water or surface states could have led to an increase of the conductivity at the surface. Second, the carrier mobility in the investigated crystals should be higher compared to the value from the literature because of the lower impurity scattering of our crystals.

The Debye screening length λ_D of the crystal was estimated from the carrier concentration using the relation [50],

$$\lambda_D = \left(\frac{\varepsilon_0 \varepsilon_r k_b T}{n e^2}\right)^{1/2}, \tag{4.2}$$

where ε_0 is the vacuum permittivity, ε_r the relative permittivity, k_b the Boltzmann constant, T the temperature, n the carrier concentration, and e the elementary charge. For ε_r the value 4 was used [51]. The resulting Debye length has a rather large value of 2.4 µm due to the low carrier concentration.

The bulk Fermi energy can be obtained from the estimate of the bulk carrier concentration [49]:

$$E_F - E_C = \ln\left[\frac{n}{2}\left(\frac{m^* k_b T}{2\pi\hbar^2}\right)^{-\frac{3}{2}}\right] k_b T, \tag{4.3}$$

where E_F is the Fermi energy, E_C the conduction band energy and m^* the effective mass of electrons in the CB. The effective mass is 0.35 m_e [52]. The expected position of the Fermi level in the bulk is therefore 0.4 eV below the CBM at room temperature (see Figure 4.2).

4.2.2. Surface States and Band Bending – Theory

Surface states in semiconductors result from breaking of the translational symmetry of the bulk. They can be either donor-like (usually closer to the VBM) or acceptor-like (usually closer to the CBM). The energy at which the gap state changes its character from predominantly donor-like to acceptor-like is the Charge Neutrality Level (CNL) of the semiconductor [53]. Depending on the position of the surface states relative to the Fermi level they can be either neutral (occupied donor-like or unoccupied acceptor-like states), charged positively (unoccupied donor-like states), or charged negatively (occupied acceptor-like states) [53]. Charged surface states cause a rearrangement of carriers close to the surface in order to screen the surface charge. This causes an upward or downward bending of the CB and VB relative to the Fermi level [4].

4.2.3. Surface States

As shown in 3.18 (a), the reduced surface shows low-lying gap states at ~2.4 eV and ~1.8 eV. These may be the In 5s states of an indium terminated surface calculated by Agoston and Albe [11], but in contrast to their suggestion, the states are completely below E_F (filled).

3.18 (b) shows the VB of the reduced surface at different photon energies. The gap states apparently decrease with increasing energy. This indicates that the gap states are located at the surface. Another interesting feature of 3.18 (b) is the decrease of the VB peak at ~8.2 eV with increasing photon energy. According to the electronic density of states (EDOS) calculations this peak should mainly arise from the In 5s states. Therefore, it represents another argument for an indium termination.

As E_F at the surface is very close to the CBM (according to PES) the state measured only with STS at E_F (Figure 3.15) could be either a surface state or the edge of the CB. We believe that it cannot be the CB edge alone because in this case we would expect a higher slope. Unfortunately, this surface state could not be confirmed by PES. There are two plausible explanations for this: First, STS is only sensitive for surface states at $\overline{\Gamma}$ ($k_{\shortparallel} = 0$). The PES analyzer had a rather wide acceptance angle of $\Theta = 12°$. The measurable parallel component with this set up can be determined by:

$$k_{\shortparallel} = \sqrt{\frac{2m_e E_{\mathrm{Kin}}}{\hbar^2}} \sin(\frac{\theta}{2}). \tag{4.4}$$

This leads to the result that areas of $k_{\shortparallel}^2\pi = 0.95\,\mathring{\mathrm{A}}^{-2}$ (photon energy: 105 eV) or $1.67\,\mathring{\mathrm{A}}^{-2}$

(photon energy 185 eV) are covered. Therefore, the analyzer collects electrons from an area larger than the first Brillouin zone (BZ): $\left(\frac{2\pi}{a}\right)^2 = 0.39\,\text{Å}^{-2}$. A state at $\overline{\Gamma}$ ($k_{\shortparallel} = 0$) might not be visible if it comprises only a small fraction of the first BZ. Assuming that the state observed by STS is located close to E_F, has a parabolic dispersion, and energy of $\triangle E$ from the bottom of the band to E_F, we can estimate the fraction of the BZ occupied by this state:

$$k_{\shortparallel} = \sqrt{\frac{2m^* \triangle E}{\hbar^2}}. \tag{4.5}$$

With an effective mass equal to that of the In_2O_3 CB ($m^* = 0.35m_e$) [52] and assuming $\triangle E = 2k_bT$ at 300 K, the area includes only ~1 % of the area measured by the PES analyzer.

The second argument is related to the cross sections: The results from Agoston and Albe suggest that the surface state probably arises from In 5s states [11]. According to the literature, the In 5s photoionization cross sections should be rather small compared to the ones for O 2p (~6.7% at 105 eV photon energy) [46]. Even at 185 eV – where the In 5s cross section is about 25% of the O 2p cross section – the surface state could not be observed.

The oxidized surface does not exhibit gap states in PES contrary to what we would have expected from the DFT calculations [11]: neither the predicted O 2s splitting and the orbital at the bottom of the VB (full peroxide termination) nor the gap states for the undercoordinated oxygen (partly peroxide surface) could be observed

Photon energy [eV]	In 5s [Mb]	O 2p [Mb]	Ratio
105	0.06	0.9	6,7%
185	0.03	0.12	25%

Table 4.1.: Photionization cross sections for In 5s and O 2p at 105 eV and 185 eV.

4.2.4. Band Bending

A more or less rigid shift of the VB (Figure 3.18 (a)) and all core levels (Figure 3.19 (a) and (b)) is usually explained by band bending. The large Debye length of 2.4 µm implies that the band bending reaches far into the bulk. This is in good agreement with the experiment, where no reduction of the band bending is observable when increasing photon energy, i.e., lowering surface sensitivity of the PES measurement. However, the carrier concentration at the surface should be higher due to the band bending (see discussion below), which would decrease the screening length.

To determine the direction of the band bending, the bulk Fermi energy (0.4 eV below the CBM) has to be regarded. The VB and the core levels of the oxidized surface are shifted by approximately the same value of 0.5 eV to lower binding energies. Assuming a fundamental band gap of 2.93 eV [7] the Fermi level is located 2.5 eV above the VBM in the bulk. At the surface, the Fermi level is pinned at 2.9 eV (2.4 eV) for the reduced (oxidized) surface above the VBM, according to the results from PES. This means the VB and the CB are bent downward by 0.4 eV for the reduced surface (Figure 4.2 (a)), and bent upward by 0.1 eV or less for the oxidized surface (Figure 4.2 (b)).

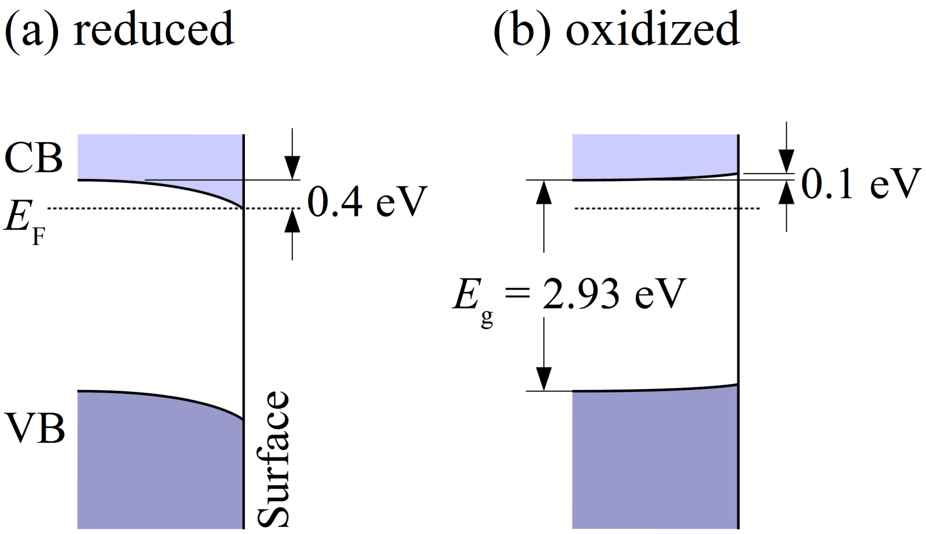

Figure 4.2.: Downward band bending of the reduced surface (a) and upwards band bending of the oxidized surface (b).

Band bending in In_2O_3 has been reported previously. King et al. described downward band bending of 0.3 eV determined by XPS measurements and carrier statistics calculations for thin films grown by Plasma-Assisted Molecular Beam Epitaxy (PAMBE) on YSZ [4]. This value was revised later to 0.45 ± 0.16 eV due to better knowledge of the band gap and an alternative method of analysis [7]. Their value is nevertheless in good agreement with our finding, where the VBM was determined by the common method of extrapolation the leading edge of the VB (see Figure 3.18 (a)). Klein observed that higher oxygen pressure during deposition leads to a lower Fermi level position in the band gap [31], which is the same trend as for our results. As he assumed a band gap of 3.6 eV, he explained the PES results with a surface depletion layer with an upward band bending of 1 eV.

For the reduced surface the gap states visible close to the VBM are filled (occupied donor-like, neutral) and cannot cause band bending. The downward band bending can be explained by positively charged, unoccupied, donor-like surface states from the excess indium atoms. They lead to an accumulation of electrons at the surface, which screen the positively charged surface state and causes the observed downward band bending. The excess indium is removed by oxidation, and the respective surface states and downward band bending disappear. The reason for the slight upward band bending, which indicates an electron depletion layer at the surface is unclear. As it is very small it might be also only an artifact caused by the uncertainties in determining the bulk Fermi level. Assuming a lower carrier concentration by a factor of 10 (as the $(1 \pm 0.2) \times 10^{12}$ cm^{-3} are an upper limit), the upward bend bending would almost disappear.

The band bending might also be another reason (beside the arguments in Section 4.2.3) why the STS surface state could no be found in PES. The STS measurement was conducted at the reduced surface. The surface state is located right at E_F and should, thus, be at least partly filled. For the oxidized surface, the bands move to lower binding energies, and the surface state moves away from E_F. Therefore, it would be no longer occupied. It is possible that the surface was less reduced (fewer sputter cycles) during the PES than during the STS measurements. Consequently the surface state was mostly unoccupied and impossible to detect by PES.

5. Summary and Outlook

The bulk and surface properties of $In_2O_3(001)$ single crystals have been investigated. The bulk measurements included polarized light microscopy, EPMA, ICP-MS, SIMS, and XRD. Polarized light microscopy of the flux-grown crystals revealed multiple growth domains and stress birefringence. The results of the EPMA-measurements led to the identification of the fluxes that were for the crystal growth. Residues of Pb, Mg and Pt were found in the In_2O_3single crystals by ICP-MS. The resistivity measurements show that the In_2O_3 single crystals can be characterized by a low carrier concentration of $\lesssim 10^{12}$ cm^{-3}. XRD measurements permitted an accurate determination of the bulk lattice constant.

The surface sensitive techniques encompassed STM, STS and PES. Sputtering and annealing in UHV up to a maximum temperature of 500 °C (higher temperatures cause an irreversible orange discoloration) likely produces indium-terminated surfaces. These are characterized by low-lying gap states at ~2.4 eV and ~1.8 eV located at the surface. The position of the VBM at a binding energy of 2.9 eV implies a strong downward band-bending by 0.4 eV. A pronounced surface state was observed in STS. STM shows the presence of wide terraces that are separated by 5 Å high step edges. The terraces are covered with 2.5 Å high regions with bright, atomic-sized features in a square pattern aligned with the [110] direction. A possible interpretation is that the terraces consist of an M-layer with small "patches" of indium atoms of the D-layer. When the surfaces are exposed to activated oxygen, the electronic structure changes. The low-lying band gap states disappear and the downward band bending is removed or even slightly reversed. A shoulder at the O 1s core level indicates the presence of peroxo species but probably not a completely dimerized termination.

In further investigations especially the influence of oxygen and water on the surface has to be investigated. The PES finding that the surface is probably partially peroxidized under oxidizing conditions should be confirmed by STM. This will be difficult, though, because of the smaller conductivity due to the absence of the surface state. According to the DFT results from Agoston and Albe exposure of the surface to water should form the most stable termination, which should look different in STM [11]. Another interesting experiment would be STS measurments of the oxidized surface to determine whether the oxidized surface really does not show a surface state as we would expect from the PES results. Furthermore, the reason why the surface state of the reduced surface could not be observed by PES should be further investigated. This could be done by measuring a new crystal with a low umber of sputtering cycles with STS or doing angle-resolved photoemission spectroscopy (ARPES). Besides, these open questions regarding the surface some bulk properties are waiting for clarification as well. Walsh et al. for example point out in a recent publication that the low-temperature thermal expansion coefficient (0 - 550 °C) has not been studied yet [54].

6. Acknowledgment

I would like to express my gratitude and appreciation to my supervisor Prof. Ulrike Diebold who gave me the opportunity to work on such an interesting topic. This work gave me an excellent insight not only in surface science, but also in the whole process of scientific work. With her highly motivational approach to supervision she encouraged me to investigate and apply a large number of experimental techniques. This culminated in the writing of a paper, which is an important milestone for me and a perfect ending for my physics studies.

I also want to thank Prof. Michael Schmid who had always an answer for every experimental or theoretical question. The interesting discussions with him greatly improved my understanding of the physics behind this work and increased the quality of this diploma thesis considerably.

Furthermore, I want to thank the rest of the group: every member of which was an outstanding colleague and helped me out with any problem. Especially I want to mention Zbyněk Novotný who introduced me to the basic experimental techniques and was an excellent teacher. Moreover, I want to thank Peter Jacobson for kindly accompanying me to the photoelectron measurements at the MAX-lab synchrotron in Lund.

Finally, I want to thank my family and my girlfriend Verena for their constant support during my studies.

Bibliography

[1] Aron Walsh and C. Catlow. Structure, stability and work functions of the low index surfaces of pure indium oxide and Sn-doped indium oxide (ITO) from density functional theory. *Journal of Materials Chemistry*, 20(46):10438, 2010.

[2] T. Bielz, H. Lorenz, W. Jochum, R. Kaindl, F. Klauser, B. Kloetzer, and S. Penner. Hydrogen on In_2O_3: Reducibility, Bonding, Defect Formation, and Reactivity. *The Journal of Physical Chemistry C*, 114(19):9022–9029, 2010.

[3] G. Korotcenkov, V. Brinzari, A. Cornet, and J. Morante. Experimental and theoretical studies of indium oxide gas sensors fabricated by spray pyrolysis. *Sensors and Actuators B: Chemical*, 106(2):563–571, May 2005.

[4] P.D.C. King, T. Veal, D. Payne, A. Bourlange, R. Egdell, and C. McConville. Surface electron accumulation and the charge neutrality level in In_2O_3. *Phys. Rev. Lett*, 101(11):116808, September 2008.

[5] Christoph Janowitz, Valentina Scherer, Mansour Mohamed, Alica Krapf, Helmut Dwelk, Recardo Manzke, Zbigniew Galazka, Reinhard Uecker, Klaus Irmscher, Roberto Fornari, Marcel Michling, Dieter Schmeiß er, Justin R Weber, Joel B Varley, and Chris G Van De Walle. Experimental electronic structure of In_2O_3 and Ga2O3. *New Journal of Physics*, 13(8):085014, August 2011.

[6] R. L. Weiher. Optical Properties of Indium Oxide. *Journal of Applied Physics*, 37(1):299, 1966.

[7] P.D.C. King, T. Veal, F. Fuchs, and C.Y. Wang. Band gap, electronic structure, and surface electron accumulation of cubic and rhombohedral In_2O_3. *Physical Review B*, 79(20):205211, May 2009.

[8] Erie H. Morales, Yunbin He, Mykola Vinnichenko, Bernard Delley, and Ulrike Diebold. Surface structure of Sn-doped In_2O_3 (111) thin films by STM. *New Journal of Physics*, 10(12):125030, December 2008.

[9] Erie H. Morales and Ulrike Diebold. The structure of the polar Sn-doped indium oxide (001) surface. *Applied Physics Letters*, 95(25):253105, 2009.

[10] A. Bourlange, D.J. Payne, R.G. Palgrave, J.S. Foord, R.G. Egdell, R.M.J. Jacobs, A. Schertel, J.L. Hutchison, and P.J. Dobson. Investigation of the growth of In_2O_3 on Y-stabilized ZrO2(100) by oxygen plasma assisted molecular beam epitaxy. *Thin Solid Films*, 517(15):4286–4294, June 2009.

[11] Peter Agoston and Karsten Albe. Thermodynamic stability, stoichiometry, and electronic structure of bcc-In_2O_3 surfaces. *Physical Review B*, 84(4):045311, July 2011.

[12] Daniel Hagleitner. Project Work: Surface Properties of Indium Oxide (100) Single Crystals, TU Wien, 2011.

[13] J. De Wit. Structural aspects and defect chemistry in In_2O_3. *Journal of Solid State Chemistry*, 20(2):143–148, February 1977.

[14] Peter Agoston and Karsten Albe. Ab initio modeling of diffusion in indium oxide. *Physical Review B*, 81(19):195205, May 2010.

[15] M. Marezio. Refinement of the crystal structure of In_2O_3 at two wavelengths. *Acta Crystallographica*, 20(6):723–728, June 1966.

[16] P.W. Tasker. The stability of ionic crystal surfaces. *Journal of Physics C: Solid State Physics*, 12:4977, 1979.

[17] Jacek Goniakowski, Fabio Finocchi, and Claudine Noguera. Polarity of oxide surfaces and nanostructures. *Reports on Progress in Physics*, 71(1):016501, January 2008.

[18] Karsten Reuter and Matthias Scheffler. Composition, structure, and stability of RuO2(110) as a function of oxygen pressure. *Physical Review B*, 65(3):035406, December 2001.

[19] Chenggang Zhou, Jiaye Li, Su Chen, Jinping Wu, Kevin R. Heier, and Hansong Cheng. First-Principles Study on Water and Oxygen Adsorption on Surfaces of Indium Oxide and Indium Tin Oxide Nanoparticles. *Journal of Physical Chemistry C*, 112(36):14015–14020, September 2008.

[20] J. De Wit. The high temperature behavior of In_2O_3. *Journal of Solid State Chemistry*, 13(3):192–200, March 1975.

[21] P. Ágoston and K. Albe. Formation entropies of intrinsic point defects in cubic In_2O_3 from first-principles density functional theory calculations. *Phys. Chem. Chem. Phys.*, 11(17):3226–3232, May 2009.

[22] G. Frank and H. Köstlin. Electrical properties and defect model of tin-doped indium oxide layers. *Applied Physics A Solids and Surfaces*, 27(4):197–206, April 1982.

[23] G. Rupprecht. Untersuchungen der elektrischen und lichtelektrischen Leitfähigkeit dünner Indiumoxydschichten. *Z. Physik*, 139:504, 1954.

[24] R. L. Weiher. Electrical Properties of Single Crystals of Indium Oxide. *Journal of Applied Physics*, 33(9):2834, 1962.

[25] Takumi Tomita, Kazuyoshi Yamashita, Yoshinori Hayafuji, and Hirohiko Adachi. The origin of n-type conductivity in undoped In_2O_3. *Applied Physics Letters*, 87(5):051911, 2005.

[26] Stephan Lany and Alex Zunger. Dopability, Intrinsic Conductivity, and Nonstoichiometry of Transparent Conducting Oxides. *Physical Review Letters*, 98(4):045501, January 2007.

[27] Julia E. Medvedeva and Chaminda L. Hettiarachchi. Tuning the properties of complex transparent conducting oxides: Role of crystal symmetry, chemical composition, and carrier generation. *Physical Review B*, 81(12):125116, March 2010.

[28] L. E. Halliburton, N. C. Giles, N. Y. Garces, Ming Luo, Chunchuan Xu, Lihai Bai, and L. A. Boatner. Production of native donors in ZnO by annealing at high temperature in Zn vapor. *Applied Physics Letters*, 87(17):172108, 2005.

[29] R. L. Weiher and B. G. Dick. Magnetoresistance of Single Crystals of Indium Oxide. *Journal of Applied Physics*, 35(12):3511, 1964.

[30] F. Fuchs and F. Bechstedt. Indium-oxide polymorphs from first principles: Quasiparticle electronic states. *Physical Review B*, 77(15):155107, April 2008.

[31] Andreas Klein. Electronic properties of In_2O_3 surfaces. *Applied Physics Letters*, 77(13):2009–2011, 2000.

[32] JP Remeika and EG Spencer. Electrical Conductivity and Growth of Single-Crystal Indium Sesquioxide. *Journal of Applied Physics*, 35(2):2803, 1964.

[33] Wolfgang Demtröder. *Experimentalphysik 2: Elektrizitat Und Optik*. Springer, 4th edition, 2006.

[34] Stephen Reed. *Electron microprobe analysis*. Cambridge Univ. Press, 2ed edition, 1997.

[35] Werner Massa. *Kristallstrukturbestimmung*. Vieweg+Teubner Verlag, 7th edition, 2011.

[36] Michael Schmid. Lecture Notes: Experimentelle Methoden der Oberflächenphysik, TU Wien, 2010.

[37] F Sanchezalmazan. Matrix effects in SIMS depth profiles of SiGe relaxed buffer layers. *Applied Surface Science*, 231-232:704–707, June 2004.

[38] Diane Beauchemin. Inductively coupled plasma mass spectrometry. *Analytical Chemistry*, 74:2873–2894, June 2002.

[39] Steven Woeste. Inductively Coupled Plasma Mass Spectrometry. *Laboratory Medicine*, 35(2):73–75, February 2004.

[40] G. Binnig, H. Rohrer, and C. Gerber. Surface studies by scanning tunneling microscopy. *Physical Review Letters*, 49(1):57–61, 1982.

[41] G. Binnig, H. Rohrer, and Ch. Gerber. Tunneling through a controllable vacuum gap. *Applied Physics Letters*, (40):178–180, 1982.

[42] J. Tersoff and D.R. Hamann. Theory of the scanning tunneling microscope. *Physical Review B*, 31(2):805, 1985.

[43] J. Bardeen. Tunneling from a many-particle point of view. *Physical Review Letters*, 6(2):57–59, 1961.

[44] S. R. Hall, H. D. Flack, and Stewart J. M. *Xtal 3.2 Reference Manual and User's Guide*. Universities of Western Australia, Geneva and Maryland, 1992.

[45] R. Nyholm, J. N. Andersen, U. Johansson, B. N. Jensen, and I. Lindau. Beamline I311 at MAX-LAB : a VUV / soft X-ray undulator beamline for high resolution electron spectroscopy. *Nuclear Instruments and Methods in Physics Research*, 468:520–524, 2001.

[46] J. J. Yeh and I. Lindau. Atomic subshell photoionization cross sections and asymmetry parameters: $1 < Z < 103$. *Atomic data and nuclear data tables*, 32(1):1–155, January 1985.

[47] S. A. Chambers, T. Droubay, T. C. Kaspar, and M. Gutowski. Experimental determination of valence band maxima for SrTiO, TiO, and SrO and the associated valence band offsets with Si(001). *Journal of Vacuum Science & Technology B: Microelectronics and Nanometer Structures*, 22(4):2205, 2004.

[48] Y. Gassenbauer and Andreas Klein. Electronic and chemical properties of tin-doped indium oxide (ITO) surfaces and ITO/ZnPc interfaces studied in-situ by photoelectron spectroscopy. *The Journal of Physical Chemistry. B*, 110(10):4793–801, March 2006.

[49] Charles Kittel. *Einführung in die Festkörperphysik*. Oldenbourg, 8th edition, 1989.

[50] Peter Y. Yu and M. Cardona. *Fundamentals of Semiconductors*. Springer, 4th edition, 2010.

[51] J. R. Bellingham, W. A. Phillips, and C. J. Adkins. Electrical and optical properties of amorphous indium oxide. *Journal of Physics: Condensed Matter*, 2(1):6207, February 1990.

[52] I. Hamberg and C.G. Granqvist. Evaporated Sn-doped In_2O_3 films: Basic optical properties and applications to energy-efficient windows. *Journal of Applied physics*, 60(11):R123–R160, 1986.

[53] Winfried Mönch. *Semiconductor Surfaces and Interfaces*. Springer, 1st edition, 1993.

[54] Aron Walsh, Alexey Sokol, and C. Catlow. Free energy of defect formation: Thermodynamics of anion Frenkel pairs in indium oxide. *Physical Review B*, 83(22):224105, June 2011.

List of Figures

List of Tables

A. Appendix

Refinement on F^2	18 parameters
$R[F^2 > 2\sigma(F^2)] = 0.016$	Weighting scheme based on measured s.u.'s $1/\ \sigma^2$
$wR(F^2) = 0.017$	$(\Delta/\sigma)\mathrm{max} = 0.20$
$S = 3.61$	$\Delta\rho\mathrm{max} = 2.66$ e Å−3
910 reflections	$\Delta\rho\mathrm{min} = -2.77$ e Å−3

Table A.1.: Refinement parameters.

In1—O1$^{\mathrm{i}}$	2.1734(2)	In2—O1	3.8167(3)
In1—O1$^{\mathrm{ii}}$	2.1734(2)	In2—O1$^{\mathrm{iii}}$	3.8167(3)
In1—O1	2.1734(2)	In2—In2$^{\mathrm{xii}}$	3.8392(1)
In1—O1$^{\mathrm{iii}}$	2.1734(2)	In2—In2	3.8392(1)
In1—O1$^{\mathrm{iv}}$	2.1734(2)	In2—In2	3.8392(1)
In1—O1$^{\mathrm{v}}$	2.1734(2)	In2—In2	3.8392(1)
In1—In2$^{\mathrm{vi}}$	3.3445(1)	In2—O1	4.0096(3)
In1—In2$^{\mathrm{vii}}$	3.3445(1)	In2—O1	4.0096(3)
In1—In2$^{\mathrm{viii}}$	3.3445(1)	In2—O1$^{\mathrm{i}}$	4.1535(3)
In1—In2$^{\mathrm{i}}$	3.3445(1)	In2—O1$^{\mathrm{xiii}}$	4.1535(3)
In1—In2$^{\mathrm{ii}}$	3.3445(1)	In2—O1	4.2583(3)
In1—In2	3.3445(1)	In2—O1	4.2583(3)
In1—In2	3.8241(1)	In2—O1	4.2766(3)
In1—In2	3.8241(1)	In2—O1	4.2766(3)
In1—In2	3.8241(1)	In2—O1	4.2912(3)
In1—In2	3.8241(1)	In2—O1	4.2912(3)
In1—In2	3.8241(1)	In2—O1$^{\mathrm{vi}}$	4.3265(3)
In1—In2	3.8241(1)	In2—O1	4.3265(3)
In1—O1	3.9926(3)	In2—O1$^{\mathrm{vii}}$	4.5346(3)
In1—O1	3.9926(3)	In2—O1$^{\mathrm{xiv}}$	4.5346(3)
In1—O1	3.9926(3)	In2—O1$^{\mathrm{xv}}$	4.7559(3)
In1—O1	3.9926(3)	In2—O1$^{\mathrm{xvi}}$	4.7559(3)
In1—O1	3.9926(3)	In2—O1	4.9599(3)
In1—O1	3.9926(3)	In2—O1	4.9599(3)
In1—O1	4.1002(3)	O1—O1	2.7986(3)
In1—O1	4.1002(3)	O1—O1	2.7986(3)
In1—O1	4.1002(3)	O1—O1$^{\mathrm{xvii}}$	2.8154(3)
In1—O1	4.1002(3)	O1—O1$^{\mathrm{vii}}$	2.8154(3)
In1—O1	4.1002(3)	O1—O1	2.9387(3)
In1—O1	4.1002(3)	O1—O1i	3.2856(3)
In1—O1$^{\mathrm{vi}}$	4.5334(3)	O1—O1	3.2856(3)
In1—O1$^{\mathrm{vii}}$	4.5334(3)	O1—O1	3.3119(3)
In1—O1$^{\mathrm{viii}}$	4.5334(3)	O1—O1	3.3119(3)
In1—O1$^{\mathrm{ix}}$	4.5334(3)	O1—O1	3.5488(3)
In1—O1$^{\mathrm{x}}$	4.5334(3)	O1—O1	3.5488(3)
In1—O1$^{\mathrm{xi}}$	4.5334(3)	O1—O1	3.7116(3)
In2—O1	2.1249(2)	O1—O1	4.1121(3)
In2—O1	2.1249(2)	O1—O1$^{\mathrm{vi}}$	4.3137(3)
In2—O1	2.1952(2)	O1—O1	4.3137(3)
In2—O1$^{\mathrm{xi}}$	2.1952(2)	O1—O1$^{\mathrm{xv}}$	4.3468(3)
In2—O1	2.2236(2)	O1—O1	4.4732(3)
In2—O1$^{\mathrm{iv}}$	2.2236(2)	O1—O1$^{\mathrm{iv}}$	4.4732(3)
In2—In2	3.3617(1)	O1—O1	4.5196(3)
In2—In2$^{\mathrm{vi}}$	3.3617(1)	O1—O1	4.6173(4)
In2—In2	3.3617(1)	O1—O1$^{\mathrm{ii}}$	4.6173(4)
In2—In2$^{\mathrm{vii}}$	3.3617(1)		

Table A.3.: Interatomic distances.

Symmetry codes: (i) z, x, y; (ii) y, z, x; (iii) −z+1/2, −x+1/2, −y+1/2; (iv) −y+1/2, −z+1/2, −x+1/2; (v) −x+1/2, −y+1/2, −z+1/2; (vi) z, −x+1/2, y+1/2; (vii) y+1/2, z, −x+1/2; (viii) −x+1/2, y+1/2, z; (ix) −z+1/2, x, −y; (x) −y, −z+1/2, x; (xi) x, −y, −z+1/2; (xii) z+1/2, −x+1/2, −y; (xiii) z, −x, −y+1/2; (xiv) y+1/2, −z, x; (xv) x+1/2, y, −z+1/2; (xvi) x+1/2, −y, z; (xvii) z+1/2, x, −y+1/2.

Site	Wyckoff Symbol	U11	U22	U33	U12	U13	U23
In1	8b	0.004290(9)	0.004290(9)	0.004290(9)	0.000580(5)	0.000580(5)	0.000580(5)
In2	24d	0.003971(11)	0.004030(10)	0.004162(10)	0	0	0.000542(5)
O	48e	0.00615(5)	0.00592(5)	0.00511(5)	-0.00046(4)	-0.00096(4)	-0.00027(4)

Table A.2.: Atomic displacement components.

General settings			
Plasma power	1200 W	Extraction lens voltage	125 V
Cooling gas flow	13 L min^{-1}	Pole bias	-1 V
Auxiliary gas flow	0.8 L min^{-1}	Hexapole bias	-4 V
Make up gas flow (Ar)	0.7 L min^{-1}		
Survey scan settings (line scan)			
Start mass	4.60 m z-1	End mass	245 m z-1
Spacing	0.2 m z-1	Dwell time	1 ms
Replicates	8		
Quantification (spots)			
Measured Isotopes	^{24}Mg, ^{90}Zr, ^{92}Zr, ^{113}In, ^{118}Sn, ^{120}Sn, ^{121}Sb, ^{126}Sb, ^{142}Nd, ^{144}Nd, ^{146}Nd, ^{194}Pt, ^{195}Pt, ^{196}Pt, ^{206}Pb, ^{207}Pb, ^{208}Pb, ^{209}Bi	Dwell time	10 ms
		Integration time	6 s
		Replicates	2 x 9

Table A.4.: ICP-MS parameters.

Line scans			
laser energy	70 %	spot size	50 µm
repetition rate	5 Hz	scan speed	5 µm s-1
Spot measurements			
laser energy	50 % and 70 %	spot size	100 µm
repetition rate	20 Hz	ablation time	10 s

Table A.5.: Laser settings for the ICP-MS.

Date	Numbers	Sputtering	Annealing	T [°C]	Dosing	Surface
11/22/10	1000-1020	10 min (2 cycles)	10 min (2 cycles)	450	-	Clean
11/23/10	1021-1040	10 min	10 min	450	-	Clean
11/24/10	1041-1049	30 min	10 min	520	-	Clean
11/25/10	1050-1096	10 min	10 min	500	-	Clean
11/26/10	1097-1113	-	1 min	550	-	Clean
11/29/10	1114-1129	10 min (2 cycles)	10 min (2 cycles)	500	-	Clean
12/1/10	1130-1131	-	-	-	-	Clean
12/1/10	1132-1135	10 min	10 min	450	-	Clean
12/2/10	1136-1171	10 min	10 min	500	-	Clean
12/7/10	1172-1188	10 min (2 cycles)	10 min (2 cycles)	500	-	Clean
12/9/10	1189-1195	10 min (2 cycles)	10 min (2 cycles)	500	-	Clean
12/13/10	1196-1201	10 min (2 cycles)	10 min (2 cycles)	500	-	Clean
12/14/10	1202-1206	10 min (2 cycles)	10 min (2 cycles)	500	-	Clean
12/15/10	1207-1226	10 min (2 cycles)	10 min (2 cycles)	600	-	Clean
12/16/10	1227-1231	-	-	-	-	Clean
12/17/10	1232-1237	-	-	-	O2-shower: 2e-6 mbar, 15 min at 500°C	Oxidized
12/21/10	1238-1241	-	-	-	O2-shower: 2e-6 mbar, 25 min at 500°C	Oxidized

Date	Numbers	Sputtering	Annealing	T [°C]	Dosing	Surface
3/24/11	37	10 min	I_EM=4.5 mA, 10 min	?	-	Clean
4/8/11	4	10 min	I_EM=3.3 mA, 10 min	?	OPA: 5.5e-6 mbar, I_E=24 mA, 10 min	Oxidized
4/11/11	13	10 min	I_EM=5 mA, 10 min	≈ 510	OPA: 5.5e-6 mbar, I_E=24 mA, 30 min	Oxidized
4/12/11	30	10 min	I_EM=5 mA, 10 min	≈ 510	-	Clean
4/13/11	28	10 min	I_EM=4.8 mA, T_Pyro=232, 10 min	448	-	Clean
4/13/11	24	10 min	I_EM=4.8 mA, T_Pyro=240, 10 min	465	OPA: 5.6e-6 mbar, I_E=24 mA, 30 min	Oxidized
4/14/11	16	10 min	I_EM=4.8 mA, T_Pyro=240, 10 min	465	OPA: 5.6e-6 mbar, I_E=24 mA, 30 min, I_EM 0.6mA	Oxidized
4/15/11	12	-	I_EM=4.8 mA, T_Pyro=234, 10 min	452	-	Oxidized
4/15/11	16	-	-	-	Evaporation: 100s, 1e-7 mbar = 10 L	Hydrogenated
4/18/11	45	10 min	I_EM=4.8 mA, T_Pyro=240, 10 min	465	Evaporation: 200s, 1e-7 mbar = 20 L	Hydrogenated
4/19/11	10	10 min	I_EM=4.8 mA, 10 min	≈ 460	-	Clean
4/19/11	37	-	-	-	Evaporation: 100s, 1e-6 mbar =100 L	Hydrogenated
4/20/11	30	10 min	I_EM=4.8 mA, 10 min	≈ 460	OPA: 5.6e-6 mbar, I_E=24 mA, 45 min, I_EM 2.3mA	Oxidized
6/9/11	20	10 min	I_EM=4.6 mA, T_Pyro0232, 10 min		OPA 5.5e-6 mbar, I_E=24mA, 30 min	Oxidized
6/9/11	6	-	I_EM=4.6 mA, 5 min	-	-	Oxidized
6/14/11	18+10	10 min	I_EM=4.6 mA, 10 min	-	OPA: 6e-6 mbar, I_E=14 mA, 30 min, I_EM 4.5mA	Oxidized
6/21/11	63+7	10 min	I_EM=4.6 mA, 10 min	-	OPA: 6e-6 mbar, I_E=14 mA, 10 min, I_EM 4.5mA	Oxidized

Date	Numbers	Sputtering	Annealing	T [°C]	Dosing	Surface
6/22/11	63+36+3	10 min	I_EM=4.7 mA, 10 min	-	OPA: 6e-6 mbar, I_E=14 mA, 10 min, I_EM 4.6mA	Oxidized
6/27/11	5	10 min	I_EM=4.8 mA, 10 min	-	OPA: 6e-6 mbar, I_E=14 mA, 10 min, I_EM 4.8mA	Oxidized
6/28/11	42	10 min	I_EM=4.8 mA, 10 min	-	OPA: 6e-6 mbar, I_E=14 mA, 40 min, I_EM 4.7mA; Flash: I_EM 4mA, 5 min	Oxidized
6/30/11	31	10 min	I_EM=4.8 mA, 10 min	-	OPA: 6e-6 mbar, I_E=14 mA, 40 min, I_EM 4.6mA; Flash: I_EM 4.7mA, 5 min	Oxidized
6/30/11	6	-	I_EM=4.8 mA, 15 min	-	-	Oxidized
7/1/11	27	-	I_EM=4.8 mA, 15 min	-	-	Oxidized

Table A.6.: Overview of STM measurements.

Spectrum #	Photon Energy [eV]	Fermi Level Correction [eV]
45	610	0.06
57	85	0.17
103	85	0.17
109	610	0.29
125	610	0.38
138	85	0.18
176	610	0.54
188	85	0.38
211	610	0.85
223	85	0.47
285	610	0.34
314	60	0.12
318	85	0.1755
318	85	0.18
322	105	0.1655
326	185	0.2155
333	610	0.24
339	60	0.16
343	85	0.16
349	105	0.15
353	185	0.19
360	610	0.14
373	85	0.17
411	610	0.28
424	85	0.17
443	60	0.15
447	85	0.17
451	105	0.19
455	185	0.26
501	60	0.12
508	85	0.17
512	105	0.17
518	610	0.32
523	60	0.3
530	85	0.36
531	105	0.36
542	60	0.4
546	85	0.45
550	105	0.48

Table A.7.: Fermi level corrections for the binding energies. Spectra have to shifted to higher binding energies.

	Reduced				Oxidized			Delta
#	Peak [eV]	E_F-Correction	Corrected	#	Peak [eV]	E_F-Correction	Corrected	
44	444.407	0.06	444.467	332	443.699	0.24	443.939	
110	444.188	0.29	444.478	359	443.931	0.14	444.071	
284	444.104	0.34	444.444	410	443.645	0.28	443.925	
515	444.282	0.32	444.602					
Average			444.49775				443.9783333	0.519416667
StdDv			0.070928955				0.080556398	

Table A.8.: Determination of the shift between the core levels of the reduced and oxidized In $3d_{5/2}$ peaks.

	Reduced				Oxidized			Delta
#	Peak [eV]	E_F-Correction	Corrected	#	Peak [eV]	E_F-Correction	Corrected	
46	529.898	0.06	529.958	334	529.228	0.24	529.468	
108	529.668	0.29	529.958	361	529.391	0.14	529.531	
516	529.76	0.32	530.08	412	529.0913	0.28	529.3713	
Average			529.9986667				529.4567667	0.5419
StdDv			0.070436732				0.080440434	

Table A.9.: Determination of the shift between the core levels of the reduced and oxidized O 1s peaks.

Peak	BE [eV]	Delta BE [eV]	Height	LFWHM	ALPHA	GFWHM	Area	Rel. Area	FWHM
1	529.09	0	26720	0.434	0	1	38940	1	1.2519
±	0.0052	0	128.9	0	0.0109	0	0.0073	0	0.0082
2	530.92	1.8373	1260	0.002	0	1.5404	2069	0.0531	1.5415
±	0.1321	0	151.1	0	0.9449	0	0.1336	0	0.391
	Background								
	A0	A1							
	6277.8	-244.06							
±	16.61	5.178							

Table A.10.: Results of the line fit of the O 1s peak. R-factor = 1.428624. LFWHM: Lorentz full width at half maximum; GFWHM: Gauss full width at half maximum; Alpha: asymmetry parameter; A0 and A1: parameters for the linear background.